Dike magmatism in the Sila Grande (Calabria, southern Italy): Evidence of Pennsylvanian–Early Permian exhumation

Vincenzo Festa[1*], Antonio Langone[2, 3], Alfredo Caggianelli[1], and Alessandro Rottura[3]
[1]*Dipartimento Geomineralogico, Università degli Studi di Bari, Via E. Orabona 4, 70125 Bari, Italy*
[2]*CNR-IGG (Consiglio Nazionale della Ricerche–Istituto di Geoscienze e Georisorse) Pavia, Via Ferrata 1, 27100 Pavia, Italy*
[3]*Dipartimento di Scienze della Terra e Geologico Ambientali, Università degli Studi Bologna, Piazza di Porta S. Donato 1, 40126 Bologna, Italy*

ABSTRACT

A dike network transecting a basement of intrusive and metamorphic rocks related to the Hercynian orogeny is exposed in the Sila Grande (southern Italy). Dike magmatism, similarly to other regions of the western Mediterranean, such as Sardinia, Corsica, and Catalonia, is of calc-alkaline to alkali-calcic affinity. Zircon U-Pb geochronology indicates that dike magmatism took place between 295 ± 1 to 277 ± 1 Ma, after the main late Hercynian emplacement of granitoids (306 ± 1 Ma). Barometry indicates that the basement underwent exhumation of 8 ± 3 km before dike injection. The dike network has a geometrical arrangement consistent with a transtensional stress regime that resulted in ductile thinning of the lower crust during the late stage of the Hercynian orogeny and concurrent fracturing of the upper crust that made possible magma ascent through dikes. The proposed tectonic evolution is related to dismemberment of the southern Hercynian belt in the central Mediterranean area as a result of dextral transtension of Gondwana in relation to Laurasia during the Pennsylvanian–Early Permian.

INTRODUCTION

The geometry, orientation, and spatial distribution of sheeted magmatic bodies (i.e., dikes and sills) are commonly used to reconstruct pathways of magma ascending through the crust. In principle, dike pattern mainly reflects the interplay between two factors: (1) the orientations of pre-existing (preemplacement) and/or syn-magmatically developed (synemplacement) tectonic discontinuities (e.g., faults and fractures), and (2) magma driving pressure. To evaluate the influence of both these factors, active subvolcanic systems can be successfully analyzed (e.g., Gudmundsson and Brenner, 2004; Gudmundsson, 2006; Tibaldi et al., 2008). The study of areas affected by ancient dike magmatism is equally important in the investigation of the significance and time of activity of tectonic discontinuity arrays. The preferential orientation of dikes is considered as symptomatic of a tectonic strain field controlling the orientation of the synemplacement faults and fractures (e.g., Glazner et al., 1999; Sadeghian et al., 2005; Dini et al., 2008), whose age of formation can be deduced by dating injected magmatic rocks. Therefore, dike swarms can be used as both age and large-scale strain markers.

Widespread dike magmatism affected the Hercynian belt of Europe during the late stages of the orogenic cycle (Wilson et al., 2004, and references therein). Dike swarms postdate most of the plutonic complexes, and are mainly related to calc-alkaline and alkaline magmatic affinity, and more rarely to tholeiitic series (Orejana et al., 2008, and references therein). In the central and western Mediterranean, dike swarms, mainly of Early Permian age, are well developed in different sectors of the southern Hercynian belt of Europe, such as the Catalan Coastal Range (Enrique, 1984, 1990; Ferrés, 1998), Corse (Rossi et al., 1993, 2002; Carmignani et al., 1999; Traversa et al., 2003; Cocherie et al., 2005), and Sardinia (Carmignani et al., 1999; Ronca et al., 1999; Atzori et al., 2000; Traversa et al., 2003) (Fig. 1). In these regions an extensional regime is considered the more appropriate tectonic context for dike magmatism (Enrique, 1984; Rossi et al., 1993; Atzori et al., 2000). Farther east, other remnants affected by dike magmatism are represented by the Sila and Serre Massifs of the Calabria-Peloritani terrane (Fig. 1), even though little is known about serial affinity, age, and tectonic framework of this magmatic event. The purpose of this paper is to close this knowledge gap through new petrological, geochronological, structural, and geochemical data collected on dikes from the central part of the Sila Massif, known as Sila Grande (Fig. 2). The main goal is to define the timing and tectonic context for magma ascent through dikes in the course of the Hercynian cycle. Petrological and geochronological results are used to estimate the amount of exhumation following an approach suggested by Ring et al. (1999). Considering that most of the Sila Grande dikes injected granodiorite (e.g., Liotta et al., 2008), depths of emplacement estimated for dikes and for the granodioritic wall rock can be combined with related intrusion ages. In addition, the analysis of dike orientations could be used to infer the tectonic strain field during exhumation. In this way the tectonic framework of dike magmatism in the course of the orogenic cycle can be successfully defined. This represents a more complete multidisciplinary approach, different from that adopted in most studies focused on dikes of the southern Hercynian belt, that rely in large amount on geochemical and geochronological data to reconstruct the tectonic setting during the late orogenic magmatism (e.g., Rossi et al., 1993; Atzori et al., 2000). Results of this research can be useful in studies devoted to recognition of geological relationships between pieces of the Hercynian basement now dispersed throughout the central Mediterranean (Alvarez and Shimabukuro, 2009).

GEOLOGICAL SETTING

A tilted, nearly complete late Hercynian continental crust section is exposed in the Sila Massif (Dubois, 1976; Graessner and Schenk, 2001). It is basically composed of three main portions; from bottom to top, these are: (1) high-grade metamorphic rocks, occupying

*Corresponding author: v.festa@geomin.uniba.it

Geosphere; October 2010; v. 6; no. 5; p. 549–566; doi: 10.1130/GES00578.1; 12 figures; 4 tables.

the Hercynian lower to middle crust; (2) nearly tabular late Hercynian granitoids, located at mid-crustal levels; and (3) low-grade metamorphic rocks belonging to the upper crust (Fig. 2).

High-grade metamorphic rocks are exposed to the west and are mainly represented by migmatitic paragneiss with intervening marble and metabasite becoming progressively more abundant toward the top. In the migmatitic paragneiss, the metamorphic assemblage of biotite + garnet + sillimanite + K-feldspar ± cordierite ± spinel equilibrated at peak pressure-temperature conditions of 400–600 Mpa and 740–770 °C (Graessner et al., 2000; Graessner and Schenk, 2001). The age of peak metamorphism, obtained by the U-Pb method on monazite, spans from ca. 305 to 296 Ma (Graessner et al., 2000).

Late Hercynian high-temperature shear deformation affected middle to lower crust in the zone straddling the contact between foliated granitoids and host migmatitic high-grade metamorphic rocks (Festa et al., 2006; Liotta et al., 2008). The compositions of granitoids range from monzogranite to tonalite (Ayuso et al., 1994), but minor mafic rocks (norite, diorite, quartz diorite) (Caggianelli et al., 1994) and strongly peraluminous leucogranite (Caggianelli et al., 2003) can be also found. Emplacement depths obtained by Al-in-hornblende barometry range from 8 to 18 km, and confirm that the intermediate crust was a preferential site for the emplacement of granitoid magmas (Caggianelli et al., 1997; Liotta et al., 2004). Using the $^{40}Ar/^{39}Ar$ method on hornblende and muscovite, Ayuso et al. (1994) estimated ages ranging from 293 to 289 Ma for these plutonic rocks. Graessner et al. (2000), using the U-Pb method on monazite, obtained emplacement ages of 304–300 Ma. Comparison of results and techniques indicates that dates by the $^{40}Ar/^{39}Ar$ method can be considered as cooling ages, by virtue of the distinctly lower closing temperatures of the involved isotopic systems (for a compilation, see Spear, 1993).

In Sila Grande, dikes transect essentially intrusive rocks but can be also found in the metamorphic basement (Fig. 3). In the earliest studies, dikes were generally related to Cenozoic volcanic activity (e.g., Rittmann, 1946; Bertolani, 1957). According to this view, some porphyritic rocks were considered to be crystallization products of lava flows. De Fino and La Volpe (1970) excluded an original subaerial setting, and recognized that emplacement of magma took place exclusively at moderate depths along subparallel fissures transecting the Paleozoic basement. Burton (1970, 1971a, 1971b, 1971c), relates dikes in the Calabria region to Paleozoic magmatic activity. One recent dating by the U-Pb method on zircon indicates an age of emplacement of 284 Ma for

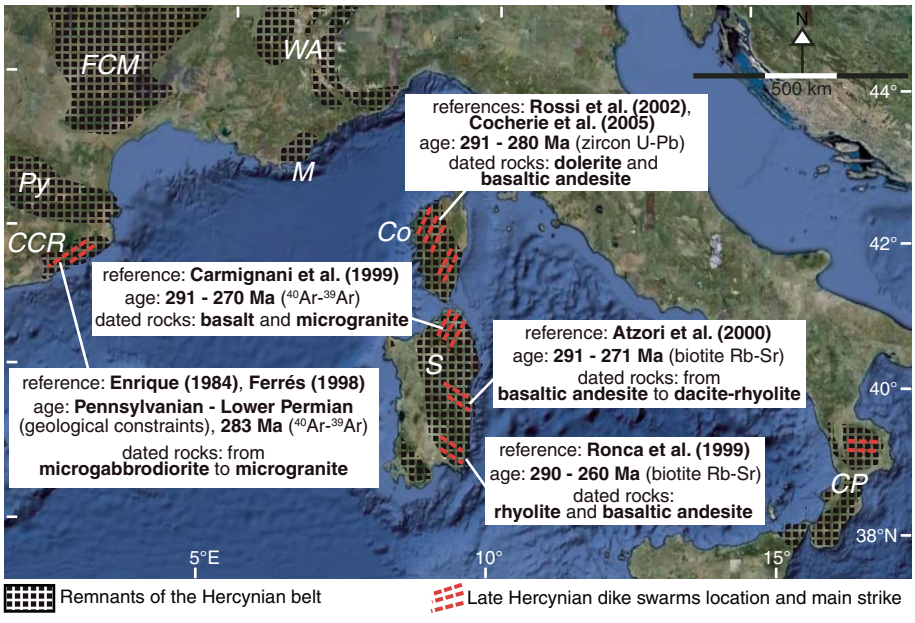

Figure 1. Pennsylvanian–Early Permian dike swarms in the regions of the central Mediterranean where remnants of the Hercynian belt crop out (CCR—Catalan Coastal Range, Py—Pyrenees, FCM—French Central Massif, WA—Western Alps, M—Maures Mountains, Co—Corse, S—Sardinia, CP—Calabria-Peloritani terrane). Rock names are as in cited references.

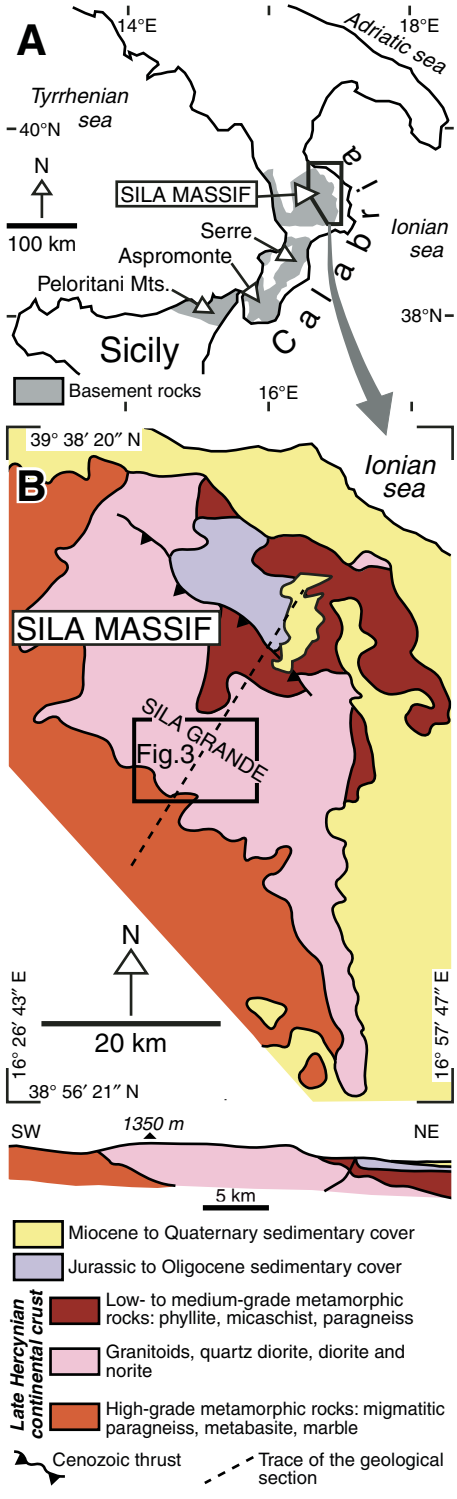

Figure 2. (A) Location of the Sila Massif in the Calabria-Peloritani terrane. (B) Geological sketch map of the Sila Massif and cross section (modified after Caggianelli and Prosser, 2001). The investigated area (see Fig. 3) is framed.

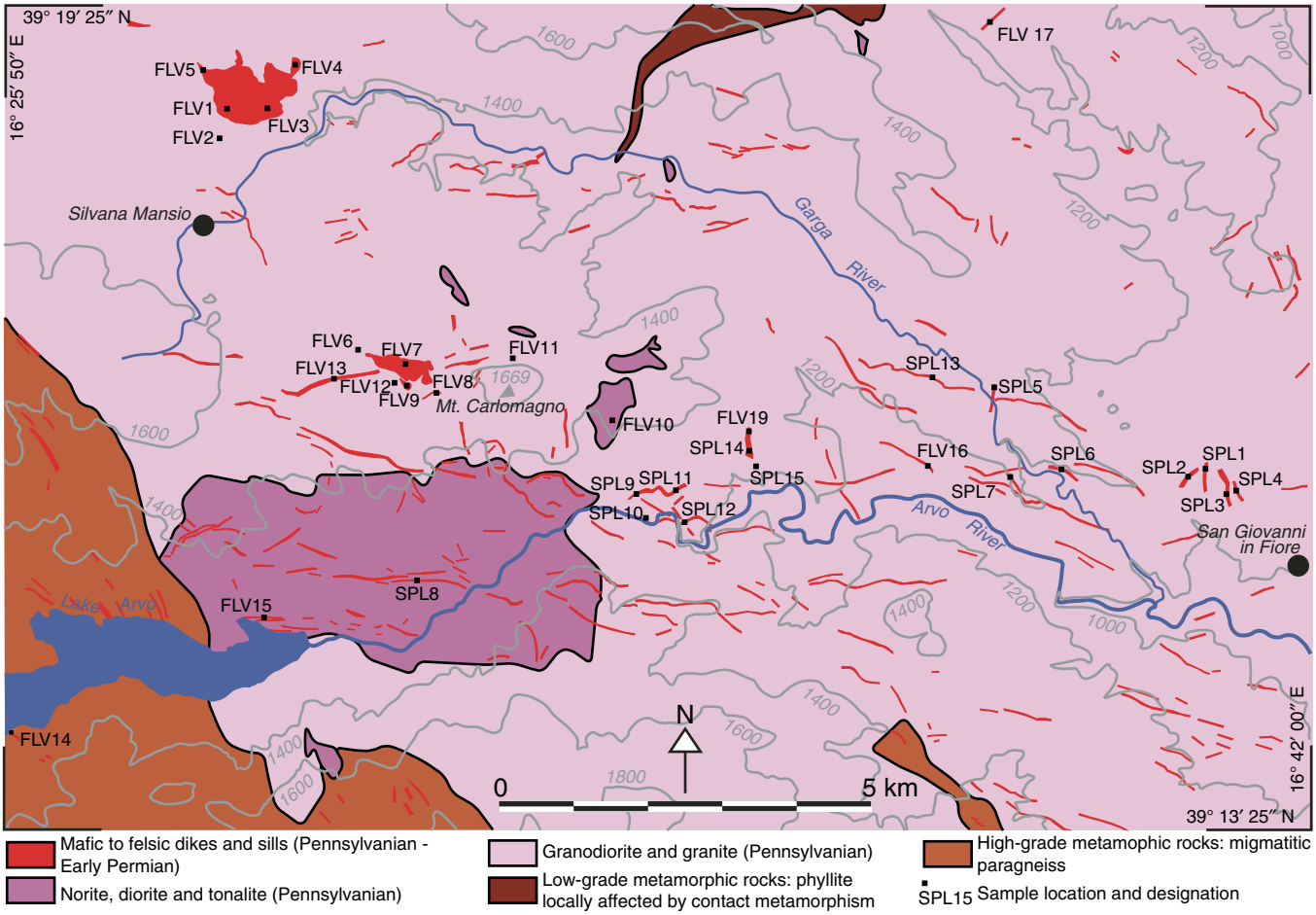

Figure 3. Geological sketch map of the Sila Grande area. Dikes are more frequent in the zone extending from Lake Arvo (west) to the town of San Giovanni in Fiore (east).

a porphyritic dike from Sila Grande (Liotta et al., 2008). This represents the only available age determination for this magmatic activity to date.

SILA GRANDE SHEETED INTRUSIONS

Distribution and Orientation

After the surveys carried out by De Fino and La Volpe (1970) and Burton (1970, 1971a, 1971b, 1971c), new intrusive bodies in the Sila Grande area were recognized, in particular within our study. In addition, the geometry of already mapped bodies is herein reinterpreted, in some instances allowing us to recognize both dikes and sills. Dikes are prevalent, and are particularly abundant in an east-west–oriented strip (5 km wide) that extends westward for 22 km from the town of San Giovanni in Fiore (Fig. 3). Sills are only represented by two subhorizontal felsic intrusions of fine-grained two-mica granite located near Silvana Mansio village and Mount Carlomagno (Fig. 3). In map view they show an irregular shape with maximum and minimum dimensions of 1.5 km and 0.8 km, respectively, and are at least ~35–40 m thick. All sheeted bodies are hosted in the Hercynian crust section, transecting mostly granitoids and more rarely the migmatitic paragneisses (Fig. 3).

A database of orientation and geometrical features has been prepared, including both new and literature field data for 353 dikes. Although some dikes are inclined, the great majority show subvertical and subplanar sharp walls. Map view suggests that most of them have a nearly tabular shape (Fig. 3). A rose diagram indicates a strong preferred orientation of dikes along an east-west strike. Other significant groups are oriented along east-southeast–west-northwest, northwest-southeast, north-northwest–south-southeast, and east-northeast–west-southwest directions (Fig. 4). Outcrop conditions are not suited to define precisely the dike extent. The maximum length estimated on the map is ~2 km (Fig. 3). However, the possibility that some dikes are

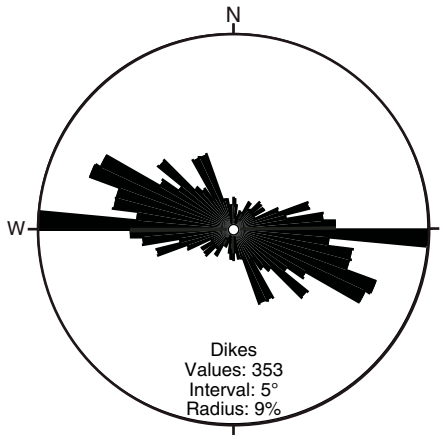

Figure 4. Rose diagram representing orientations of dikes from Sila Grande.

part of a longer, single sheeted body cannot be excluded. The thickness of some dikes (up to ~15 m) argues for a length decidedly >2 km according to the typical thickness/length ratio of dikes in the upper crust of 0.01, given by Lister and Kerr (1991).

Petrography and Chemical Classification

The Sila Grande dikes display a notable compositional variety, as evidenced by the presence of both felsic and mafic types. Felsic dikes are more frequently exposed, and are represented by microgranite and microgranodiorite. In these rocks plagioclase ranges from albite to An-poor oligoclase, and biotite is the only mafic mineral. In microgranite scarce biotite coexists with white mica, whereas in microgranodiorite biotite occurs in larger amounts, and white mica is absent or rare. In the more felsic dikes, quartz and K-feldspar are frequently present in granophyric texture. Accessory magmatic minerals are represented by columnar to acicular apatite and zircon, whereas sphene, chlorite, and opaque minerals appear to be of postmagmatic origin.

Mafic dikes are made up of dark fine-grained rocks consisting of plagioclase, quartz, green amphibole, biotite, and rare augite. An abundance of amphibole, together with the labradorite composition of plagioclase ($An_{55–70}$), indicates that these rocks are intermediate between microdiorite and microgabbro. For this reason the name "microgabbrodiorite" is adopted here. Accessory minerals include opaque minerals, columnar to acicular apatite, and zircon, whereas epidote, chlorite, and calcite are considered to be of postmagmatic origin.

Textures in both felsic and mafic dikes are commonly porphyritic, but in some cases (especially in microgranodiorite and microgranite) approach an equigranular type (Figs. 5A–5C), as is typical of felsite. The gradual increase of grain size from the margins inward is a common feature in dikes (Figs. 5D and 5E). Clear evidence of multiple magma injections, such as internal contact and irregular grain size distribution, were not observed. On this basis, the dikes appear to be the product of a single magma intrusion event.

Furthermore, a relation of near parallelism between margins, and the elongation of subhedral feldspars, up to 1 mm in length, is observed in some dikes, and particularly in microgranodiorites where flow texture is sometimes observed (Fig. 6A). Quenching textures are represented in felsic dikes by feldspar and biotite spherulites (Fig. 6B), and in mafic dikes by ocelli consisting of hornblende microlites often radiating around resorbed quartz xeno-

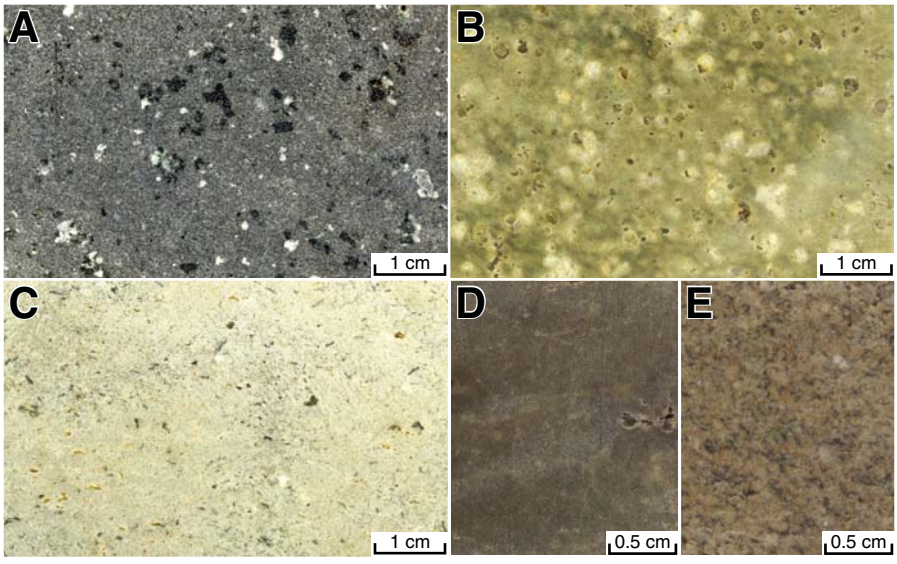

Figure 5. Scanner images of rock slabs. (A) Typical porphyritic texture in microgabbrodiorite (sample SPL14). (B) Typical porphyritic texture in porphyritic microgranite (sample FLV13). (C) A lower grain-size contrast between phenocrystals and matrix minerals can be observed in microgranite (sample FLV17). (D, E) Increase of grain size from margin (D, sample FLV16S) to center (E, sample FLV16I) in a microgranite dike.

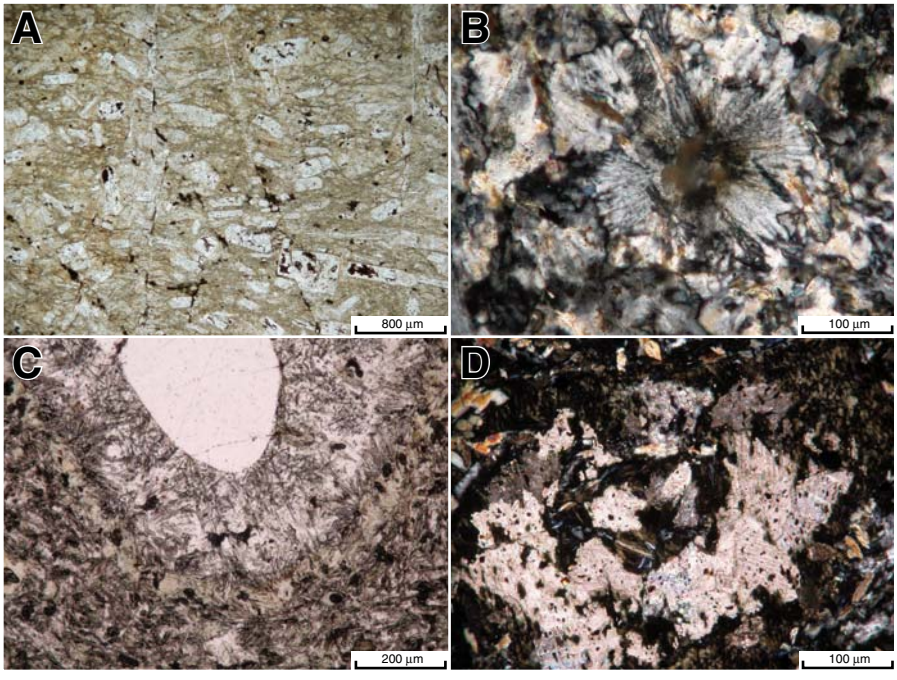

Figure 6. Thin-section microphotographs. (A) Preferred orientation of feldspars in microgranodiorite (plane polarized light, sample SPL1). (B) Feldspar spherulite in a microgranite dike (crossed polars, sample SPL12). (C) Acicular hornblendes around ovoidal quartz (crossed polars, sample FLV19). An outer shell of pale green chlorite can be also observed. (D) Amygdule filled by alternating calcite and chlorite shells (crossed polars, sample SPL14).

crysts (Fig. 6C). Additional evidence of fast cooling of magma is suggested by the common elongated shapes of micas and of acicular amphibole and apatite. Textures related to fluid exsolution are represented in mafic dikes by amygdules. They are filled by calcite or by alternating chlorite and calcite shells, and have a maximum diameter of 3 mm (Fig. 6D). Amygdules occupy ~1% rock volume.

The chemical compositions of the sampled felsic and mafic magmatic rocks are given in Table 1. Chemical classification according to the TAS (total-alkali-silica) diagram is proposed in Figure 7A. Dikes display a wide compositional range from basaltic andesite to rhyolite, and are mainly represented by dacite and rhyolite. In comparison to host calc-alkaline granitoids, dike magmatism drifts toward trends of alkali-calcic serial affinity (Frost et al., 2001) (Fig. 7B), characterized by a moderately high Na_2O content (Fig. 7C), consistent with late orogenic to postorogenic timing.

Rare earth element patterns, from the results of the analyses shown in Table 2, are provided for three dikes and host granodiorite. All patterns are fractionated, with Ce_N/Yb_N increasing from the mafic (Ce_N/Yb_N = 6.69) to the felsic types (8.55 and 12.66) and to granodiorite (14.26). A negative Eu anomaly increases in magnitude from the mafic (Eu/Eu* = 0.747) to felsic compositions (0.508 and 0.345), with granodiorite having an intermediate value (0.611) (Fig. 7D). These variations are compatible with a variable extent of plagioclase and amphibole fractionation. The spider diagram in Figure 7E shows a significant depletion in K, Ta, Nb, Sr, and, Ti for all rock samples. A major role of plagioclase in magma-fractionation processes is confirmed by the more pronounced Sr negative spike observed in felsic dikes.

LEVEL OF EMPLACEMENT

Most dikes transect granitoids, and this suggests that magma ascent reached at least the intermediate level of the continental crustal section. However, relevant textural features indicate an even shallower level of emplacement, and a significant time lag from the intrusion of the main granitoids. Magma quenching textures, such as alkali-feldspar spherulites (Fig. 6B), acicular hornblende around quartz ocelli (Fig. 6C), and vesiculation textures, such as amygdules (Fig. 6D), point to fast magma cooling at a shallow crustal level. In addition, the presence of amygdules, restricted to mafic dikes, is in agreement with the lower solubility of volatiles in basic melts with respect to acidic melts.

TABLE 1. WHOLE-ROCK MAJOR AND TRACE ELEMENT COMPOSITION OF FELSIC AND MAFIC DIKES

	Felsic dikes																Mafic dikes			
wt%	SPL1	SPL2	SPL3	SPL4	SPL5a	SPL5b	SPL6a	SPL6b	SPL7a	SPL7b	SPL8	SPL9	SPL11	SPL12a	SPL12b	SPL13	FLV7	FLV13	FLV16	FLV17	SPL10	SPL14a	SPL14b	FLV19
SiO_2	67.30	66.08	69.39	67.73	70.79	73.76	67.19	69.15	65.89	66.00	74.15	73.86	74.53	73.99	75.27	72.47	73.03	76.42	70.59	73.44	60.03	52.72	53.73	54.05
TiO_2	0.42	0.53	0.36	0.35	0.21	0.21	0.48	0.36	0.57	0.57	0.01	0.12	0.12	0.12	0.12	0.20	0.18	0.10	0.23	0.08	0.80	1.10	1.18	1.07
Al_2O_3	17.35	16.57	15.68	18.32	16.24	15.03	16.08	15.44	17.50	16.93	15.17	14.69	14.30	14.62	13.71	15.17	14.70	12.50	16.18	14.69	15.52	15.01	15.05	15.29
FeO_{total}	4.39	4.59	3.89	3.88	2.28	2.08	4.40	3.90	4.42	4.55	1.23	1.82	1.78	1.85	1.90	2.26	1.72	1.45	2.17	1.84	6.59	9.29	9.28	8.75
MnO	0.04	0.06	0.06	0.02	0.02	0.01	0.05	0.06	0.05	0.05	0.01	0.02	0.02	0.02	0.03	0.04	0.06	0.05	0.07	0.07	0.11	0.13	0.14	0.16
MgO	1.51	1.31	0.90	0.90	0.65	0.55	1.11	0.71	0.83	1.16	0.00	0.02	0.02	0.00	0.01	0.50	0.33	0.11	0.83	0.19	7.17	8.76	8.69	7.48
CaO	0.55	1.74	0.71	0.20	0.66	0.43	2.13	1.98	1.64	1.64	0.35	0.38	0.33	0.37	0.69	1.26	0.61	0.14	0.53	0.14	1.79	5.77	5.88	6.07
Na_2O	4.19	4.96	4.34	3.64	4.22	3.70	4.43	4.42	4.30	4.43	4.32	4.19	4.01	4.07	3.76	4.21	2.92	4.44	4.84	4.36	3.69	2.57	2.12	3.34
K_2O	2.26	2.85	3.09	2.77	3.47	3.06	2.78	2.94	2.92	3.07	4.09	4.27	4.14	4.28	4.17	3.24	5.56	4.07	3.23	4.06	1.08	1.24	1.63	1.35
P_2O_5	0.09	0.16	0.08	0.04	0.07	0.05	0.15	0.10	0.16	0.16	0.00	0.02	0.01	0.01	0.02	0.07	0.25	0.03	0.13	0.05	0.47	0.31	0.28	0.35
L.O.I.	1.88	1.15	1.51	2.14	1.38	1.11	1.20	0.93	1.73	1.45	0.67	0.61	0.75	0.68	0.33	0.59	0.63	0.68	1.19	1.07	2.75	3.09	2.02	2.09
ppm																								
Rb	143	115	114	138	142	147	124	119	126	121	227	195	182	198	199	138	413	199	118	188	35	48	66	38
Sr	81	156	132	127	85	107	208	210	189	166	27	73	76	63	64	127	60	49	108	54	743	332	317	322
Y	48	27	26	34	20	19	28	29	27	28	18	28	27	23	29	20	27	62	19.9	23.4	19	30	31	31.4
Zr	345	321	407	391	152	152	313	382	332	315	43	142	146	141	148	155	90	127	156	111	285	255	257	243
Nb	12	12	11	12	8	9	12	11	12	11	12	12	11	11	12	8	13	21	6.8	9.4	14	12	12	11.9
Ce	79	74	91	57	52	41	73	81	79	71	18	63	61	56	77	49	24	28	57.5	95.4	112	78	77	73.7
La	45	36	47	53	28	25	39	42	40	41	13	38	44	31	41	28	15	7	27.3	34.5	51	40	35	35.6
Ba	183	378	377	325	307	335	383	380	393	409	111	395	409	382	376	305	183	66	371	495	457	520	474	695
Ni	3	4	4	2	6	6	5	5	4	3	5	4	4	5	5	9	7	4	8	4	107	65	68	53
V	16	21	6	8	5	4	22	7	24	22	2	2	2	2	0	6	8	2	10	3	119	158	160	167

Note: Major and trace elements concentrations were determined by X-ray fluorescence spectrometry at Dipartimento Geomineralogico, University of Bari. Counts were converted in weight percent (wt%) and parts per million (ppm) by matrix correction method according to Franzini et al. (1975). Trace element contents from Rb to Ba for the samples FLV16l, FLV17, and FLV19 were determined by inductively coupled plasma–mass spectrometry (see also Table 2).

In a tentative attempt to define quantitatively the emplacement level, a petrological approach was adopted. A depth estimate was obtained by combining Al-in-hornblende barometry (Anderson and Smith, 1995) with hornblende-plagioclase thermometry (Holland and Blundy, 1994). This approach was applied both for a mafic dike and for the granodiorite wall rock (Table 3). In the mafic dike, amphibole composition in the groundmass ranges from edenite to hornblende, whereas plagioclase is labradorite ($An_{59–69}$). Simultaneous solution of the barometric and thermometric (edenite-richterite exchange) equations allowed us to estimate a level of emplacement for the mafic dike of 5 ± 2 km (pressure, P = 130 ± 60 MPa). In granodiorite, amphibole rims are edenitic hornblende, and plagioclase rims are andesine ($An_{39–45}$). By the same approach, we calculated a level of emplacement for granodiorite of 13 ± 2 km (350 ± 60 MPa). Results are considered reliable, because the pressure-temperature equilibrium values (130 ± 60 MPa at 840 ± 40 °C and 350 ± 60 MPa at 760 ± 40 °C) plot beyond wet solidus conditions for andesite to basalt (Wyllie, 1978; Green, 1982) and for a granodiorite (Schmidt and Thompson, 1996), respectively. Therefore, the significant difference in emplacement depths indicates that intrusion of the mafic dike took place after considerable exhumation of the host granodiorite, that, according to the more conservative choice allowed by error ranges, is not <4 km. In addition, as indicated by the presence of amygdules, basic magma reached saturation in volatiles somewhere during ascent. Saturations at the pressure-temperature conditions of the emplacement level both in H_2O and CO_2 can be set by VolatileCalc software (Newman and Lowenstern, 2002), and are, respectively, 3.3 wt% and 600 ppm for a basaltic magma. These are minimum estimates for original volatile content of the magma. By lowering magma density, volatiles may have been the determining factor in favoring magma ascent up to shallow crustal levels. If water was the dominant volatile, as suggested by the elevated content of hydrous minerals, then it contributed also to depression of the liquidus temperature, allowing a considerable cooling of magma before full crystallization (Sisson et al., 1996).

AGE OF DIKE MAGMATISM

Owing to outcrop conditions, no geological method can be applied with confidence to infer the emplacement sequence of the various dikes. Thus geochronology is the only option to shed light on this subject. To this end, we selected three different dike samples representative of the main compositional and textural types. In addition, we dated a granodiorite wall rock to define the time lag of dike magmatism with respect to the main late Hercynian magmatic event.

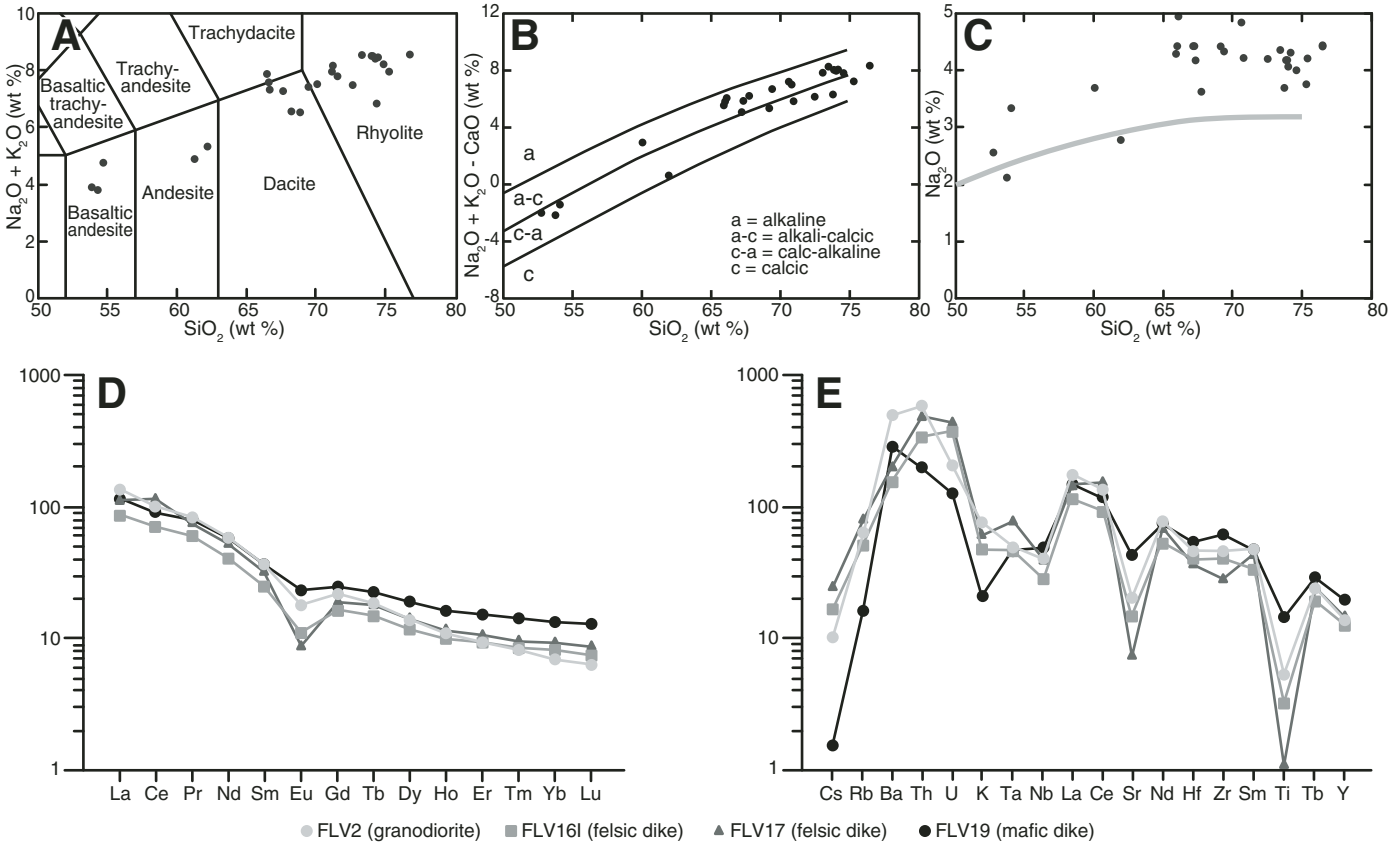

Figure 7. Compositional characteristics of the studied dikes based on major oxides. (A) Chemical classification of the dikes in the TAS (total-alkali-silica) diagram (analyses recalculated anhydrous following Le Bas et al., 1986). (B) Chemical classification of dikes in terms of rock series according to the modified alkali-lime index (MALI) by Frost et al. (2001). (C) Na_2O versus SiO_2 diagram showing dike data points in comparison to the trend (gray curve by polynomial regression) of host Pennsylvanian plutonic rocks (Caggianelli et al., 1994). Compositional characteristics are based on trace elements for three dikes, and one host granodiorite. (D) Rare earth element patterns (chondrite normalizing values after Boynton, 1984). (E) Spider diagram (chondrite normalizing values after McDonough and Sun, 1995).

TABLE 2. TRACE ELEMENT CONTENTS FOR SELECTED SAMPLES

	Granodiorite	Felsic dikes		Mafic dike
ppm	FLV2	FLV16I	FLV17	FLV19
La	42.0	27.3	34.5	35.6
Ce	82.7	57.5	95.4	73.7
Pr	10.40	7.31	9.16	9.88
Nd	35.7	24.7	31.6	34.9
Sm	7.23	4.95	6.38	7.25
Eu	1.32	0.77	0.65	1.72
Gd	5.79	4.23	4.99	6.56
Tb	0.88	0.70	0.85	1.07
Dy	4.58	3.85	4.72	6.16
Ho	0.80	0.72	0.85	1.18
Er	2.01	1.98	2.26	3.29
Tm	0.26	0.28	0.32	0.46
Yb	1.50	1.74	1.95	2.85
Lu	0.21	0.24	0.28	0.42
Cs	2.0	3.2	4.8	0.3
Rb	147	118	188	38
Ba	1200	371	495	695
Th	17.10	9.74	14.00	5.84
U	1.48	2.60	3.11	0.89
Ta	0.71	0.66	1.09	0.65
Nb	10.0	6.8	9.4	11.9
Sr	150	108	54	322
Hf	4.8	4.2	3.8	5.7
Zr	176	156	111	243
Tl	0.85	0.62	1.10	0.10
Y	22.2	19.9	23.4	31.4

Note: Trace element chemistry was performed by Activation Laboratories Ltd. (Canada), and determined by inductively coupled plasma–mass spectrometry on the fusion solution; ppm—parts per million.

TABLE 3. COMPOSITION OF AMPHIBOLE AND PRESSURE-TEMPERATURE ESTIMATES

	Granodiorite SPL15 Rim		Mafic dike FLV19 Microlites					
Weight percent								
SiO_2	43.77	42.93	46.90	48.99	49.06	48.02	43.90	44.43
TiO_2	1.40	1.19	1.33	1.27	1.29	1.42	1.83	1.91
Al_2O_3	9.02	9.70	7.57	6.80	5.25	6.72	10.52	9.15
FeO	18.74	19.54	20.02	18.10	16.10	18.99	18.25	18.68
MnO	0.67	0.39	0.10	0.52	0.40	0.36	0.26	0.31
MgO	9.39	9.43	9.00	10.26	12.29	10.85	9.91	10.55
CaO	11.92	11.55	10.60	9.28	10.72	9.31	10.18	9.54
Na_2O	1.85	2.00	2.27	1.92	1.89	2.44	2.74	2.64
K_2O	0.98	1.00	0.43	1.11	0.32	0.33	0.69	0.45
Total	97.74	97.72	98.22	98.23	97.32	98.44	98.29	97.67
	ΣO = 23		ΣO = 23					
Si	6.627	6.494	6.993	7.213	7.222	7.029	6.510	6.595
Ti	0.159	0.135	0.149	0.140	0.143	0.156	0.204	0.213
Al	1.611	1.731	1.332	1.181	0.912	1.161	1.841	1.603
Fe	2.372	2.472	2.496	2.224	1.982	2.324	2.263	2.318
Mn	0.086	0.049	0.013	0.065	0.050	0.045	0.033	0.039
Mg	2.119	2.125	2.000	2.253	2.697	2.367	2.191	2.333
Ca	1.934	1.872	1.693	1.465	1.691	1.460	1.617	1.517
Na	0.543	0.587	0.656	0.548	0.539	0.692	0.786	0.759
K	0.189	0.193	0.082	0.208	0.060	0.062	0.131	0.086
cations	15.641	15.659	15.414	15.298	15.295	15.296	15.577	15.463
*P (MPa)	369	339	106	147	143	135	112	114
†T (°C)	743	781	811	764	845	873	871	909

Note: Analyses were done on by a Cambridge S360 scanning electron microscope equipped with a LINK AN 10000 ED (energy dispersive) detector (Consiglio Nazionale della Ricerche, Chimica dei Plasmi instrument hosted in Dipartimento Geomineralogico, University of Bari, Italy). Operating conditions were 15 kV accelerating potential, 1 nA probe current. For standardization were used several minerals and pure compounds manufactured by Micro-Analysis Consultants Ltd. (www.macstandars.co.uk).

*P (pressure) estimates were obtained by Al-in-hornblende barometry according to the Anderson and Smith (1995) equation.

†T (temperature) estimates were obtained with hornblende-plagioclase thermometry (Holland and Blundy, 1994) assuming equilibrium with An_{41} and An_{64} plagioclase for granodiorite and in the mafic dike, respectively.

Methodology

Zircons were concentrated using standard mineral separation techniques from fresh representative samples of ~3–6 kg. Zircons free from cracks were preferentially selected, mounted in epoxy resin, and polished to obtain the exposure of their maximum surface along the c-axis. Grains were examined with cathodoluminescence (CL) imaging techniques using the JEOL scanning electron microscope at the CNR-IGG (Consiglio Nazionale della Ricerche–Istituto di Geoscienze e Georisorse), Unità di Pavia (Italy). CL images of zircons were used in order to select the most suitable location of the analytical spots for U-Pb geochronology (Fig. 8).

Age determinations of zircons were performed (CNR-IGG, Unità di Pavia) using a 193 nm ArF excimer laser ablation microprobe (GeoLas200QMicrolas) coupled to a magnetic sector inductively coupled plasma–mass spectrometer (Element from ThermoFinnigan). The analytical details are given in Tiepolo (2003). Analyses were carried out in single spot mode and with a spot size of ~25 μm. The laser was operated with a frequency of 5 Hz and with a fluence of 12 J cm^{-2}. Mass bias and laser induced fractionation were corrected by adopting zircon 91500 (1062.4 ± 0.4 Ma; Wiedenbeck et al., 1995) as the external standard. The same spot size and integration intervals were considered on both standard and studied samples. Data reduction was carried out through the GLITTER software package (van Achterbergh et al., 2001). Time-resolved signals were carefully inspected to detect perturbation of the signal related to inclusions, cracks, or mixed age domains. Within the same analytical run, the error associated with the reproducibility of the external standard was propagated to each analysis (see Horstwood et al., 2003), and after this procedure each age determination was accurate within the quoted error. The concordia test was performed for each analytical spot from $^{206}Pb/^{238}U$ and $^{207}Pb/^{235}U$

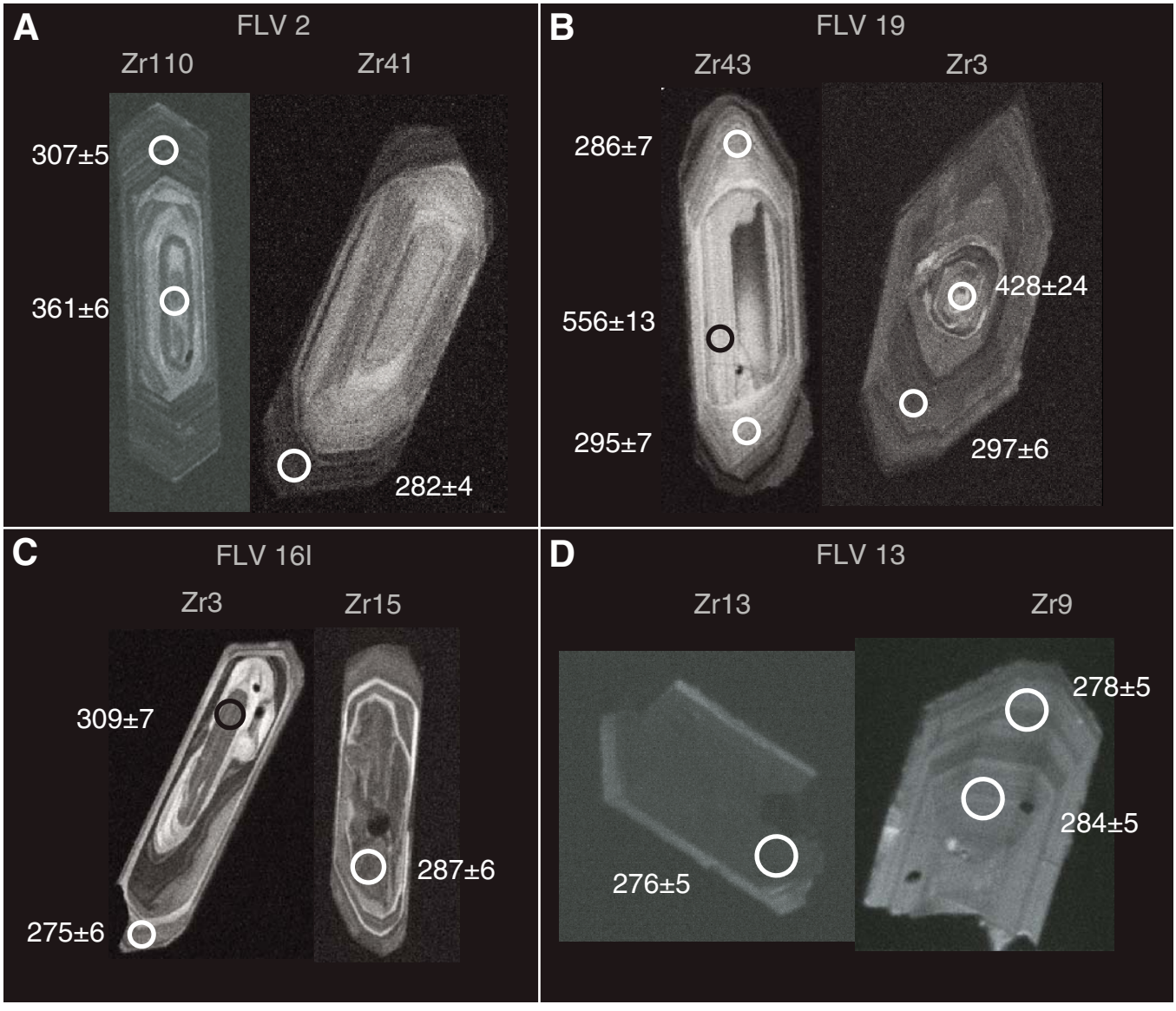

Figure 8. Representative cathodoluminescent (CL) microphotographs of zircons. The location and size of LA-ICP-MS (laser ablation–inductively coupled plasma–mass spectrometer) spot analyses, their concordant ages (in Ma), and 2σ uncertainties are indicated. Circles represent spot analyses, with a diameter of ca. 25 μm.

ratios using the function in the software package Isoplot/Ex3.00 (Ludwig, 2003). Concordia ages and associated 2σ errors are reported in Table 4. The discordant data were not taken into consideration because of doubtful interpretation. The Isoplot/Ex3.00 software was also used to draw probability density plots and concordia diagrams (Fig. 9).

Analytical Results and Age Interpretations

Ages were interpreted in light of internal features (Fig. 8). Euhedral, concentric, oscillatory zones have been considered as evidence of magmatic growth (Paterson et al., 1989; Vavra, 1990; Miller et al., 1992; Hanchar and Miller, 1993). Inner zones with truncations and/or with abrupt changes of the zoning pattern with respect to the surrounding areas have been interpreted as inherited domains.

Sample FLV2 (Granodiorite)

FLV2 is characterized by very large zircons, often having dimensions of ~200 × 80 µm (3.2 aspect ratio). Crystals preferentially developed the steep pyramid forms in longitudinal sections. Usually, the zircons contain inclusions and the larger crystals are fractured.

CL images of ~110 crystals revealed that the zircons are very luminescent. They show a well-developed growth zoning with pronounced fine oscillatory zoned bands. In some cases these bands enclose one large uniform central zone. Generally, the outer part of the crystals is less luminescent with respect to the inner part. Zircons could contain small rounded inclusions of apatite and/or inherited cores (Zr110; Fig. 8A). In few cases, the oscillatory zoning is interrupted by discontinuities (Fig. 8A).

We collected 52 U-Pb data from 43 different crystals; 36 U-Pb analyses on oscillatory zoning domains yield concordant ages ranging from 326 ± 6 Ma to 272 ± 5 Ma (Table 4; Fig. 9), whereas a single spot on the core yields an U-Pb concordia age of 361 ± 6 Ma (Fig. 8A), suggesting an inherited origin for this core. U-Pb concordia ages show a major cluster with weighted average age of 306 ± 1 Ma (mean square of weighted deviates, MSWD = 0.81, probability = 0.70; n = 20), and two minor clusters ca. 325 and 280 Ma (Fig. 9). The two ages of ca. 325 Ma refer to bright oscillatory cores surrounded by dark oscillatory rims, and thus they have been interpreted as inherited ages. The younger ages of ca. 280 Ma may be the result of partial U-Pb resetting due to a subsequent tectonometamorphic event.

Sample FLV 19 (Mafic Dike)

Zircons in this sample show well-developed prismatic faces with steep pyramidal terminations. The typical dimensions range from 100 to 200 µm in length, and from 40 to 80 µm in width with aspect ratios between 2 and 4. Generally, the zircons are very luminescent. Rarely, low luminescent crystals or areas are visible. CL images revealed well-developed oscillatory growth zoning without significant luminescence variations from core toward rims. In few cases, zircons contain small rounded inclusions and/or inherited cores (Fig. 8B).

We collected 50 U-Pb data from 36 different crystals; 45 U-Pb analyses yield concordant ages ranging from 313 ± 7 Ma to 273 ± 8 Ma (Fig. 9), and three ages were 556 ± 13 Ma, 428 ± 24 Ma, and 353 ± 8 Ma (Table 4). These three older ages clearly correspond to inherited cores. A large population of U-Pb concordia ages defines a prominent peak in the density diagrams ca. 296 Ma with a weighted average age of 295 ± 1 Ma (MSWD = 0.93, probability = 0.56; n = 24) (Table 4; Fig. 9).

Sample FLV 16I (Felsic Dike)

Combining optical observations with CL images, zircons in this sample are characterized by longitudinal sections with well-developed prismatic faces and flat pyramidal terminations. The dominant dimensions are ~140 × 50 µm (aspect ratio = 3) with rare cases of 250 × 50 µm. CL images revealed that they are very luminescent with variable intensity from outer toward inner portions. The oscillatory growth zoning from core toward rims is a typical internal feature of the crystals, and is locally interrupted by discontinuities related to dissolution. Inherited cores showing internal features discordant with respect to the regular growth zoning of the surrounding rims rarely occur. Alternatively, they can be spongy or may show irregular zoning (Fig. 8C).

We collected 50 U-Pb data from 37 different crystals; 20 U-Pb analyses yield concordant ages ranging from 309 ± 6 Ma to 266 ± 6 Ma, with a single value at 393 ± 9 Ma. The larger population of U-Pb data defines a major and minor cluster ca. 278 Ma and 304 Ma, respectively. The ages of the major cluster refer mainly to rims with well-developed oscillatory zoning or to cores of zircon grains showing continuous oscillatory zoning, and have a weighted average age of 278 ± 2 Ma (MSWD = 0.69, probability = 0.70; n = 9) (Table 4; Fig. 9). The ages of the minor cluster refer mainly to core with different luminescence properties with respect to the rims, except for two data obtained from near-rim domains enclosed within the dissolution surface. According to zircon internal features and to U-Pb data, the older ages refer to the zircon core and/or domain of inherited origin. The inherited ages are coherent with the dominant ages of the granodiorite.

Sample FLV 13 (Felsic Dike)

In accordance with the lower grain size in the entire matrix, zircons are smaller than those of the other samples, with dimensions ranging from 150 µm × 100 µm to 65 µm × 50 µm. Optical and cathodoluminescent investigations revealed that the zircon grains have longitudinal sections with well-developed prismatic faces, and poorly developed flat pyramidal terminations. CL images indicate that the zircons are weakly luminescent, and do not show a pronounced oscillatory growth zoning. In some cases, outer domains are more luminescent with respect to the inner domains, and, rarely, inverse luminescence properties have been observed (Fig. 8D).

We collected 34 U-Pb data from 21 different crystals; 15 U-Pb analyses yield concordant ages ranging from 284 ± 5 Ma to 260 ± 4 Ma with a major concordant population with weighted average age of 277 ± 1 Ma (MSWD = 0.58, probability = 0.86; n = 13) (Table 4; Fig. 9).

On the basis of these data, the Sila Grande can be interpreted to be the result of a sequence of late Hercynian magmatic events, starting with emplacement of granodiorite at 306 ± 1 Ma, followed by the injection of the mafic dikes at 295 ± 1 Ma, and ending with the felsic dikes at 277 ± 1 Ma.

DISCUSSION AND CONCLUSIONS

Tectonic Exhumation of the Sila Grande Basement

Results obtained in this study can be used to constrain amount of exhumation of the Sila basement from Pennsylvanian to Early Permian time. Toward this end, depths of emplacement estimated for the mafic dike and for the granodioritic wall rock are combined with related emplacement ages. Assuming that intrusion of the mafic dike took place with a time lag of 11 ± 1 m.y. with respect to granodiorite, and that the difference in emplacement depth amounts to 8 ± 3 km, an average exhumation rate of 0.7 ± 0.3 mm/yr is estimated. This value can be compared with the duration of the late Hercynian decompression documented for Hercynian lower continental crust exposed in Calabria. According to Schenk (1989) and Graessner and Schenk (2001), the lower crust underwent decompression of 200–140 MPa in a time span of 10 m.y. (from 300 to 290 Ma; Schenk, 1989). These data indicate an exhumation rate of 0.5–0.7 mm/yr. Therefore, the late Hercynian exhumation documented here for the upper crust is consistent with the decompression rate of the lower crust.

Given that dike magmatism and exhumation were simultaneous, we examine here the question of whether tectonic deformation is the main

TABLE 4. ISOTOPIC RATIOS AND AGE ESTIMATES

Analysis	Sample	Zircon	Position	Isotopic ratios								Concordia ages	
				$^{206}Pb/^{238}U$	±1σ (%)	$^{207}Pb/^{235}U$	±1σ (%)	$^{207}Pb/^{206}Pb$	±1σ (%)	$^{208}Pb/^{232}Th$	±1σ (%)	Age (Ma)	±2σ (Ma)
Se03c005	FLV2	1	rim	0.0492	0.04	0.3565	0.70	0.0525	0.12	0.0146	0.03	310	5
Se03c009	FLV2	6	core	0.0519	0.05	0.3787	0.91	0.0528	0.14	0.0146	0.04	326	6
Se03c010	FLV2	9	rim	0.0442	0.03	0.3136	0.45	0.0516	0.09	0.0135	0.03	279	4
Se03c011	FLV2	10	rim	0.0442	0.03	0.3153	0.46	0.0518	0.10	0.0141	0.03	279	4
Se03c012	FLV2	10	core	0.0487	0.04	0.3517	0.73	0.0525	0.12	0.0141	0.03	306	5
Se03c013	FLV2	13	rim	0.0490	0.05	0.3546	0.97	0.0523	0.16	0.0157	0.04	308	6
Se03c014	FLV2	13	rim	0.0485	0.05	0.3505	1.22	0.0526	0.20	0.0128	0.03	305	6
Se03c015	FLV2	13	core	0.0471	0.04	0.3370	0.69	0.0518	0.12	0.0153	0.03	297	5
Se03c017	FLV2	18	rim	0.0490	0.04	0.3540	0.76	0.0524	0.13	0.0166	0.04	309	5
Se03c018	FLV2	19	rim	0.0491	0.04	0.3466	0.61	0.0513	0.11	0.0156	0.04	309	5
Se03c019	FLV2	22	rim	0.0431	0.04	0.3057	0.83	0.0515	0.15	0.0134	0.03	272	5
Se03c020	FLV2	29	rim	0.0492	0.05	0.3541	1.25	0.0520	0.20	0.0203	0.06	310	6
Se03c021	FLV2	26	rim	0.0442	0.03	0.3111	0.46	0.0511	0.10	0.0127	0.03	278	4
Se03c022	FLV2	27	core	0.0450	0.05	0.3209	1.22	0.0516	0.21	0.0139	0.04	284	6
Se03c023	FLV2	36	rim	0.0430	0.04	0.3136	0.78	0.0528	0.15	0.0136	0.04	272	5
Se03c024	FLV2	36	rim	0.0449	0.04	0.3194	0.59	0.0516	0.11	0.0142	0.04	283	5
Se03c025	FLV2	41	rim	0.0447	0.03	0.3162	0.39	0.0513	0.09	0.0150	0.03	282	4
Se03c026	FLV2	39	rim	0.0487	0.04	0.3453	0.69	0.0516	0.12	0.0152	0.04	307	5
Se03c028	FLV2	42	rim	0.0486	0.04	0.3486	0.52	0.0518	0.10	0.0141	0.03	306	5
Se03c030	FLV2	56	rim	0.0490	0.04	0.3468	0.51	0.0515	0.10	0.0131	0.03	308	4
Se03c031	FLV2	59	core	0.0460	0.03	0.3302	0.54	0.0522	0.11	0.0140	0.03	290	4
Se03c036	FLV2	62	rim	0.0486	0.04	0.3511	0.46	0.0525	0.09	0.0145	0.03	306	4
Se03c037	FLV2	68	core	0.0485	0.04	0.3489	0.50	0.0520	0.10	0.0145	0.03	305	4
Se03c040	FLV2	80	rim	0.0455	0.04	0.3269	0.41	0.0522	0.09	0.0133	0.03	287	4
Se03c041	FLV2	80	rim	0.0453	0.03	0.3204	0.41	0.0514	0.09	0.0142	0.03	285	4
Se03c044	FLV2	87	core	0.0491	0.04	0.3548	0.61	0.0525	0.11	0.0159	0.04	309	5
Se03c046	FLV2	89	core	0.0516	0.05	0.3668	0.79	0.0519	0.13	0.0155	0.03	324	6
Se03c047	FLV2	91	core	0.0484	0.05	0.3446	0.82	0.0520	0.14	0.0138	0.03	304	6
Se03c048	FLV2	94	rim	0.0486	0.04	0.3504	0.78	0.0523	0.13	0.0149	0.03	306	5
Se03c049	FLV2	95	core	0.0479	0.04	0.3502	0.57	0.0531	0.11	0.0137	0.03	302	5
Se03c051	FLV2	100	rim	0.0443	0.04	0.3127	0.82	0.0514	0.15	0.0133	0.03	279	5
Se03c052	FLV2	101	rim	0.0481	0.04	0.3512	0.46	0.0530	0.09	0.0142	0.03	303	5
Se03c053	FLV2	102	rim	0.0439	0.03	0.3130	0.47	0.0516	0.10	0.0123	0.03	277	4
Se03c054	FLV2	105	rim	0.0487	0.04	0.3517	0.48	0.0524	0.09	0.0154	0.03	306	4
Se03c056	FLV2	104	rim	0.0482	0.04	0.3496	0.50	0.0528	0.10	0.0141	0.03	304	4
Se03c057	FLV2	110	rim	0.0488	0.04	0.3517	0.45	0.0526	0.09	0.0145	0.03	307	5
Se03c058	FLV2	110	core	0.0576	0.05	0.4230	0.86	0.0537	0.13	0.0181	0.04	361	6
Se02a005	FLV19	3	core	0.0689	0.20	0.5744	3.37	0.0605	0.12	0.0220	0.09	428	24
Se02a006	FLV19	3	rim	0.0472	0.05	0.3394	0.60	0.0522	0.10	0.0155	0.03	297	7
Se02a007	FLV19	2	rim	0.0467	0.05	0.3345	0.60	0.0520	0.10	0.0157	0.03	294	7
Se02a008	FLV19	5	rim	0.0461	0.05	0.3322	0.68	0.0524	0.11	0.0140	0.03	290	7
Se02a009	FLV19	6	rim	0.0446	0.05	0.3142	0.55	0.0511	0.09	0.0118	0.02	281	6
Se02a013	FLV19	10	core	0.0563	0.07	0.4149	0.94	0.0536	0.13	0.0223	0.06	353	8
Se02a015	FLV19	12	rim	0.0467	0.05	0.3356	0.63	0.0522	0.10	0.0191	0.04	294	6
Se02a016	FLV19	13	rim	0.0483	0.06	0.3527	0.92	0.0530	0.14	0.0147	0.03	304	7
Se02a017	FLV19	16	rim	0.0462	0.05	0.3325	0.66	0.0522	0.11	0.0140	0.02	291	7
Se02a018	FLV19	16	core	0.0488	0.06	0.3516	0.70	0.0523	0.11	0.0133	0.02	307	7
Se02a019	FLV19	19	rim	0.0498	0.06	0.3612	0.92	0.0527	0.14	0.0153	0.03	313	7
Se02a020	FLV19	19	core	0.0497	0.06	0.3607	0.73	0.0527	0.11	0.0158	0.03	312	7
Se02a021	FLV19	24	core	0.0448	0.05	0.3305	0.73	0.0537	0.12	0.0123	0.02	283	6
Se02a022	FLV19	23	core	0.0477	0.05	0.3432	0.68	0.0523	0.11	0.0155	0.03	300	7
Se02a023	FLV19	20	rim	0.0485	0.05	0.3507	0.63	0.0525	0.10	0.0172	0.03	305	7
Se02a024	FLV19	20	core	0.0499	0.06	0.3617	0.73	0.0526	0.11	0.0131	0.02	313	7
Se02a025	FLV19	21	rim	0.0472	0.05	0.3421	0.63	0.0526	0.10	0.0160	0.03	297	6
Se02a026	FLV19	22	core	0.0474	0.05	0.3436	0.68	0.0526	0.11	0.0132	0.02	298	7
Se02a027	FLV19	28	core	0.0470	0.05	0.3387	0.66	0.0523	0.11	0.0148	0.02	296	7
Se02a028	FLV19	27	rim	0.0464	0.06	0.3347	0.78	0.0524	0.13	0.0141	0.03	292	7
Se02a029	FLV19	27	rim	0.0436	0.05	0.3123	0.68	0.0519	0.12	0.0137	0.02	275	6
Se02a031	FLV19	26	rim	0.0433	0.06	0.3079	1.45	0.0516	0.25	0.0144	0.08	273	8
Se02a035	FLV19	25	core	0.0475	0.06	0.3434	0.80	0.0524	0.13	0.0140	0.02	299	7
Se02a036	FLV19	25	rim	0.0461	0.05	0.3336	0.76	0.0525	0.13	0.0138	0.02	290	7
Se02a037	FLV19	25	core	0.0493	0.08	0.3538	1.78	0.0522	0.27	0.0120	0.05	310	9
Se02a038	FLV19	29	core	0.0488	0.06	0.3523	0.98	0.0523	0.15	0.0153	0.03	307	7
Se02a039	FLV19	35	core	0.0470	0.06	0.3428	0.88	0.0531	0.14	0.0160	0.04	296	7
Se02a040	FLV19	37	rim	0.0480	0.06	0.3455	1.32	0.0523	0.21	0.0146	0.04	302	8
Se02a041	FLV19	37	rim	0.0461	0.05	0.3306	0.70	0.0520	0.11	0.0135	0.02	290	7

(*Continued*)

TABLE 4. ISOTOPIC RATIOS AND AGE ESTIMATES (*Continued*)

Analysis	Sample	Zircon	Position	Age estimates								Concordia ages	
				$^{206}Pb/^{238}U$ (Ma)	±1σ (Ma)	$^{207}Pb/^{235}U$ (Ma)	±1σ (Ma)	$^{207}Pb/^{206}Pb$ (Ma)	±1σ (Ma)	$^{208}Pb/^{232}Th$ (Ma)	±1σ (Ma)	Age (Ma)	±2σ (Ma)
Se03c005	FLV2	1	rim	310	2	310	6	309	7	293	6	310	5
Se03c009	FLV2	6	core	326	3	326	8	318	9	294	8	326	6
Se03c010	FLV2	9	rim	279	2	277	4	266	5	271	5	279	4
Se03c011	FLV2	10	rim	279	2	278	4	275	5	282	6	279	4
Se03c012	FLV2	10	core	306	3	306	6	306	7	282	6	306	5
Se03c013	FLV2	13	rim	308	3	308	8	298	9	315	8	308	6
Se03c014	FLV2	13	rim	305	3	305	11	312	12	257	6	305	6
Se03c015	FLV2	13	core	297	2	295	6	276	7	306	6	297	5
Se03c017	FLV2	18	rim	309	3	308	7	303	7	333	8	309	5
Se03c018	FLV2	19	rim	309	3	302	5	253	5	313	7	309	5
Se03c019	FLV2	22	rim	272	3	271	7	263	8	268	6	272	5
Se03c020	FLV2	29	rim	309	3	308	11	285	11	407	12	310	6
Se03c021	FLV2	26	rim	279	2	275	4	243	5	256	5	278	4
Se03c022	FLV2	27	core	284	3	283	11	267	11	278	7	284	6
Se03c023	FLV2	36	rim	272	2	277	7	318	9	272	8	272	5
Se03c024	FLV2	36	rim	283	2	281	5	268	6	286	7	283	5
Se03c025	FLV2	41	rim	282	2	279	3	256	4	301	6	282	4
Se03c026	FLV2	39	rim	307	3	301	6	266	6	304	8	307	5
Se03c028	FLV2	42	rim	306	2	304	4	278	5	283	6	306	5
Se03c030	FLV2	56	rim	308	2	302	4	262	5	264	5	308	4
Se03c031	FLV2	59	core	290	2	290	5	294	6	281	6	290	4
Se03c036	FLV2	62	rim	306	2	306	4	306	5	292	6	306	4
Se03c037	FLV2	68	core	305	2	304	4	285	5	291	6	305	4
Se03c040	FLV2	80	rim	287	2	287	4	295	5	267	5	287	4
Se03c041	FLV2	80	rim	285	2	282	4	257	4	285	6	285	4
Se03c044	FLV2	87	core	309	2	308	5	306	6	318	7	309	5
Se03c046	FLV2	89	core	324	3	317	7	279	7	310	7	324	6
Se03c047	FLV2	91	core	305	3	301	7	283	7	276	6	304	6
Se03c048	FLV2	94	rim	306	3	305	7	297	8	300	7	306	5
Se03c049	FLV2	95	core	302	2	305	5	331	7	274	6	302	5
Se03c051	FLV2	100	rim	279	2	276	7	260	8	267	6	279	5
Se03c052	FLV2	101	rim	303	2	306	4	330	6	284	6	303	5
Se03c053	FLV2	102	rim	277	2	276	4	270	5	248	6	277	4
Se03c054	FLV2	105	rim	306	2	306	4	301	5	308	6	306	4
Se03c056	FLV2	104	rim	304	2	304	4	321	6	283	6	304	4
Se03c057	FLV2	110	rim	307	2	306	4	311	5	291	6	307	5
Se03c058	FLV2	110	core	361	3	358	7	357	8	363	8	361	6
Se02a005	FLV19	3	core	429	12	461	27	623	12	440	18	428	24
Se02a006	FLV19	3	rim	297	3	297	5	295	5	311	6	297	7
Se02a007	FLV19	2	rim	294	3	293	5	284	5	314	5	294	7
Se02a008	FLV19	5	rim	290	3	291	6	301	6	282	5	290	7
Se02a009	FLV19	6	rim	281	3	277	5	244	5	237	4	281	6
Se02a013	FLV19	10	core	353	4	352	8	352	8	445	12	353	8
Se02a015	FLV19	12	rim	294	3	294	5	293	6	382	8	294	6
Se02a016	FLV19	13	rim	304	4	307	8	329	9	295	6	304	7
Se02a017	FLV19	16	rim	291	3	291	6	295	6	281	5	291	7
Se02a018	FLV19	16	core	307	4	306	6	300	6	267	4	307	7
Se02a019	FLV19	19	rim	313	4	313	8	315	8	307	6	313	7
Se02a020	FLV19	19	core	312	4	313	6	316	7	316	5	312	7
Se02a021	FLV19	24	core	282	3	290	6	356	8	248	4	283	6
Se02a022	FLV19	23	core	301	3	300	6	297	6	311	6	300	7
Se02a023	FLV19	20	rim	305	3	305	5	307	6	345	7	305	7
Se02a024	FLV19	20	core	314	4	314	6	312	7	262	4	313	7
Se02a025	FLV19	21	rim	297	3	299	5	310	6	321	7	297	6
Se02a026	FLV19	22	core	298	3	300	6	312	6	265	5	298	7
Se02a027	FLV19	28	core	296	3	296	6	297	6	296	5	296	7
Se02a028	FLV19	27	rim	292	3	293	7	303	7	283	6	292	7
Se02a029	FLV19	27	rim	275	3	276	6	283	6	275	5	275	6
Se02a031	FLV19	26	rim	273	4	273	13	266	13	288	17	273	8
Se02a035	FLV19	25	core	299	3	300	7	301	7	280	5	299	7
Se02a036	FLV19	25	rim	290	3	292	7	306	7	277	5	290	7
Se02a037	FLV19	25	core	310	5	308	16	292	15	241	9	310	9
Se02a038	FLV19	29	core	307	4	306	9	298	9	307	6	307	7
Se02a039	FLV19	35	core	296	4	299	8	333	9	321	7	296	7
Se02a040	FLV19	37	rim	302	4	301	11	298	12	293	8	302	8
Se02a041	FLV19	37	rim	290	3	290	6	287	6	271	5	290	7

(*Continued*)

TABLE 4. ISOTOPIC RATIOS AND AGE ESTIMATES (*Continued*)

Analysis	Sample	Zircon	Position	Isotopic ratios								Concordia ages	
				$^{206}Pb/^{238}U$	±1σ (%)	$^{207}Pb/^{235}U$	±1σ (%)	$^{207}Pb/^{206}Pb$	±1σ (%)	$^{208}Pb/^{232}Th$	±1σ (%)	Age (Ma)	±2σ (Ma)
Se02a042	FLV19	36	core	0.0462	0.06	0.3299	0.97	0.0520	0.16	0.0126	0.02	291	7
Se02a043	FLV19	36	core	0.0476	0.05	0.3427	0.74	0.0523	0.12	0.0141	0.03	299	7
Se02a044	FLV19	39	rim	0.0475	0.06	0.3432	1.14	0.0526	0.18	0.0156	0.04	299	8
Se02a045	FLV19	40	rim	0.0474	0.06	0.3422	0.76	0.0525	0.12	0.0141	0.03	299	7
Se02a047	FLV19	43	rim	0.0454	0.06	0.3268	1.13	0.0523	0.19	0.0147	0.04	286	7
Se02a048	FLV19	43	rim	0.0469	0.06	0.3401	1.16	0.0526	0.19	0.0151	0.04	295	7
Se02a049	FLV19	43	core	0.0902	0.11	0.7218	2.19	0.0582	0.18	0.0276	0.07	556	13
Se02a050	FLV19	49	rim	0.0449	0.05	0.3230	0.63	0.0522	0.11	0.0130	0.02	283	6
Se02a051	FLV19	50	rim	0.0462	0.05	0.3310	0.60	0.0520	0.10	0.0139	0.03	291	6
Se02a052	FLV19	54	core	0.0487	0.06	0.3532	0.86	0.0526	0.13	0.0131	0.03	306	7
Se02a053	FLV19	54	rim	0.0484	0.06	0.3470	1.04	0.0518	0.16	0.0138	0.03	304	7
Se02a055	FLV19	57	core	0.0471	0.05	0.3391	0.67	0.0522	0.11	0.0141	0.02	296	7
Se02a056	FLV19	58	rim	0.0474	0.06	0.3419	1.05	0.0525	0.17	0.0148	0.03	298	7
Se02a057	FLV19	59	core	0.0465	0.06	0.3330	0.88	0.0523	0.14	0.0133	0.02	293	7
Se02a059	FLV19	61	rim	0.0474	0.05	0.3410	0.62	0.0522	0.10	0.0104	0.02	298	6
Se02a061	FLV19	61	rim	0.0468	0.06	0.3368	1.17	0.0525	0.19	0.0127	0.02	294	8
se02b006	FLV16l	3	rim	0.0437	0.05	0.3101	0.41	0.0516	0.08	0.0137	0.03	275	6
se02b007	FLV16l	3	core	0.0490	0.06	0.3568	0.56	0.0529	0.10	0.0135	0.03	309	7
se02b008	FLV16l	4	core	0.0481	0.06	0.3504	0.56	0.0529	0.10	0.0156	0.04	303	7
se02b009	FLV16l	4	rim	0.0444	0.05	0.3179	0.35	0.0520	0.07	0.0140	0.03	281	4
se02b010	FLV16l	9	rim	0.0456	0.05	0.3277	0.42	0.0521	0.08	0.0140	0.03	288	6
se02b012	FLV16l	10	core	0.0439	0.05	0.3142	0.39	0.0520	0.08	0.0119	0.02	277	6
se02b015	FLV16l	8	rim	0.0453	0.06	0.3337	0.67	0.0534	0.12	0.0144	0.03	286	7
se02b017	FLV16l	15	core	0.0456	0.05	0.3255	0.42	0.0518	0.08	0.0149	0.03	287	6
se02b019	FLV16l	16	rim	0.0471	0.06	0.3420	0.61	0.0527	0.11	0.0133	0.03	297	7
se02b021	FLV16l	16	rim	0.0437	0.05	0.3116	0.47	0.0517	0.09	0.0144	0.03	276	6
se02b028	FLV16l	22	rim	0.0481	0.06	0.3480	0.63	0.0526	0.11	0.0140	0.03	303	7
se02b040	FLV16l	55	rim	0.0443	0.05	0.3159	0.41	0.0518	0.08	0.0130	0.02	279	6
se02b042	FLV16l	58	core	0.0436	0.05	0.3118	0.49	0.0518	0.09	0.0130	0.03	275	7
se02b044	FLV16l	59	core	0.0441	0.05	0.3136	0.47	0.0516	0.09	0.0135	0.03	278	7
se02b045	FLV16l	64	core	0.0421	0.05	0.2996	0.40	0.0516	0.08	0.0130	0.03	266	6
se02b046	FLV16l	64	core	0.0441	0.05	0.3154	0.45	0.0518	0.09	0.0132	0.02	278	7
se02b051	FLV16l	73	core	0.0628	0.08	0.4707	0.77	0.0544	0.10	0.0191	0.04	393	9
se02b053	FLV16l	82	rim	0.0446	0.05	0.3138	0.50	0.0510	0.09	0.0134	0.03	281	7
se02b055	FLV16l	85	core	0.0484	0.06	0.3494	0.42	0.0524	0.08	0.0144	0.03	304	6
se02b057	FLV16l	87	core	0.0470	0.06	0.3436	0.56	0.0531	0.10	0.0142	0.03	297	7
oc10d005	FLV13	1	core	0.0437	0.04	0.3117	0.54	0.0522	0.09	0.0136	0.03	276	5
oc10d006	FLV13	1	rim	0.0440	0.04	0.3066	0.53	0.0509	0.09	0.0128	0.03	277	5
oc10d009	FLV13	3	rim	0.0436	0.04	0.3115	0.51	0.0518	0.08	0.0136	0.03	275	5
oc10d011	FLV13	5	rim	0.0441	0.04	0.3144	0.53	0.0517	0.09	0.0131	0.03	278	5
oc10d014	FLV13	8	rim	0.0440	0.04	0.3116	0.59	0.0515	0.10	0.0125	0.03	277	5
oc10d015	FLV13	8	rim	0.0442	0.04	0.3144	0.53	0.0517	0.09	0.0130	0.03	279	5
oc10d016	FLV13	9	rim	0.0441	0.04	0.3140	0.56	0.0518	0.09	0.0139	0.03	278	5
oc10d017	FLV13	9	core	0.0450	0.04	0.3312	0.57	0.0533	0.09	0.0135	0.03	284	5
oc10d020	FLV13	11	rim	0.0435	0.04	0.3140	0.52	0.0523	0.09	0.0130	0.03	275	5
oc10d026	FLV13	13	rim	0.0438	0.04	0.3141	0.49	0.0523	0.08	0.0127	0.03	276	5
oc10d028	FLV13	14	core	0.0442	0.04	0.3131	0.58	0.0516	0.10	0.0128	0.03	278	5
oc10d030	FLV13	15	core	0.0433	0.03	0.3119	0.47	0.0522	0.08	0.0125	0.03	274	4
oc10d034	FLV13	18	core	0.0412	0.04	0.2934	0.53	0.0517	0.09	0.0120	0.03	260	4
oc10d035	FLV13	19	core	0.0442	0.03	0.3138	0.50	0.0515	0.08	0.0131	0.03	279	4
oc10d038	FLV13	22	core	0.0441	0.04	0.3140	0.75	0.0531	0.13	0.0128	0.03	278	5

(*Continued*)

TABLE 4. ISOTOPIC RATIOS AND AGE ESTIMATES (*Continued*)

Analysis	Sample	Zircon	Position	Age estimates								Concordia ages	
				$^{206}Pb/^{238}U$ (Ma)	±1σ (Ma)	$^{207}Pb/^{235}U$ (Ma)	±1σ (Ma)	$^{207}Pb/^{206}Pb$ (Ma)	±1σ (Ma)	$^{208}Pb/^{232}Th$ (Ma)	±1σ (Ma)	Age (Ma)	±2σ (Ma)
Se02a042	FLV19	36	core	291	4	290	8	287	9	253	5	291	7
Se02a043	FLV19	36	core	299	3	299	6	298	7	283	5	299	7
Se02a044	FLV19	39	rim	299	4	300	10	312	11	313	7	299	8
Se02a045	FLV19	40	rim	299	3	299	7	305	7	283	5	299	7
Se02a047	FLV19	43	rim	286	4	287	10	296	11	294	7	286	7
Se02a048	FLV19	43	rim	295	4	297	10	313	11	303	8	295	7
Se02a049	FLV19	43	core	557	7	552	17	535	17	550	14	556	13
Se02a050	FLV19	49	rim	283	3	284	6	292	6	260	4	283	6
Se02a051	FLV19	50	rim	291	3	290	5	283	5	279	6	291	6
Se02a052	FLV19	54	core	306	4	307	8	310	8	263	5	306	7
Se02a053	FLV19	54	rim	304	4	302	9	277	9	277	5	304	7
Se02a055	FLV19	57	core	296	3	296	6	296	6	283	5	296	7
Se02a056	FLV19	58	rim	299	4	299	9	306	10	297	6	298	7
Se02a057	FLV19	59	core	293	4	292	8	298	8	268	5	293	7
Se02a059	FLV19	61	rim	298	3	298	5	295	6	208	3	298	6
Se02a061	FLV19	61	rim	295	4	295	10	309	11	255	5	294	8
se02b006	FLV16l	3	rim	276	3	274	4	266	4	275	5	275	6
se02b007	FLV16l	3	core	308	4	310	5	323	6	270	5	309	7
se02b008	FLV16l	4	core	303	4	305	5	326	6	312	7	303	7
se02b009	FLV16l	4	rim	280	3	280	3	284	4	281	5	281	4
se02b010	FLV16l	9	rim	288	3	288	4	291	5	280	5	288	6
se02b012	FLV16l	10	core	277	3	277	3	285	4	239	4	277	6
se02b015	FLV16l	8	rim	286	4	292	6	348	8	290	6	286	7
se02b017	FLV16l	15	core	288	3	286	4	275	4	298	6	287	6
se02b019	FLV16l	16	rim	297	4	299	5	316	6	267	5	297	7
se02b021	FLV16l	16	rim	276	3	275	4	273	5	289	6	276	6
se02b028	FLV16l	22	rim	303	4	303	5	311	6	280	6	303	7
se02b040	FLV16l	55	rim	279	3	279	4	276	4	261	5	279	6
se02b042	FLV16l	58	core	275	3	276	4	277	5	262	5	275	7
se02b044	FLV16l	59	core	278	3	277	4	270	5	272	5	278	7
se02b045	FLV16l	64	core	266	3	266	4	269	4	261	5	266	6
se02b046	FLV16l	64	core	278	3	278	4	278	5	265	5	278	7
se02b051	FLV16l	73	core	393	5	392	6	388	7	382	8	393	9
se02b053	FLV16l	82	rim	281	3	277	4	242	4	269	5	281	7
se02b055	FLV16l	85	core	305	4	304	4	304	4	290	5	304	6
se02b057	FLV16l	87	core	296	4	300	5	331	6	286	6	297	7
oc10d005	FLV13	1	core	276	2	275	5	292	5	273	6	276	5
oc10d006	FLV13	1	rim	278	2	272	5	236	4	257	6	277	5
oc10d009	FLV13	3	rim	275	2	275	4	278	5	274	6	275	5
oc10d011	FLV13	5	rim	278	2	278	5	272	5	264	6	278	5
oc10d014	FLV13	8	rim	277	3	275	5	263	5	251	6	277	5
oc10d015	FLV13	8	rim	279	2	278	5	273	5	261	6	279	5
oc10d016	FLV13	9	rim	278	2	277	5	276	5	279	6	278	5
oc10d017	FLV13	9	core	284	3	291	5	340	6	272	6	284	5
oc10d020	FLV13	11	rim	275	2	277	5	299	5	261	6	275	5
oc10d026	FLV13	13	rim	276	2	277	4	299	5	255	6	276	5
oc10d028	FLV13	14	core	279	2	277	5	267	5	258	6	278	5
oc10d030	FLV13	15	core	274	2	276	4	292	4	250	6	274	4
oc10d034	FLV13	18	core	260	2	261	5	270	5	241	6	260	4
oc10d035	FLV13	19	core	279	2	277	4	264	4	262	6	279	4
oc10d038	FLV13	22	core	278	3	277	7	331	8	257	6	278	5

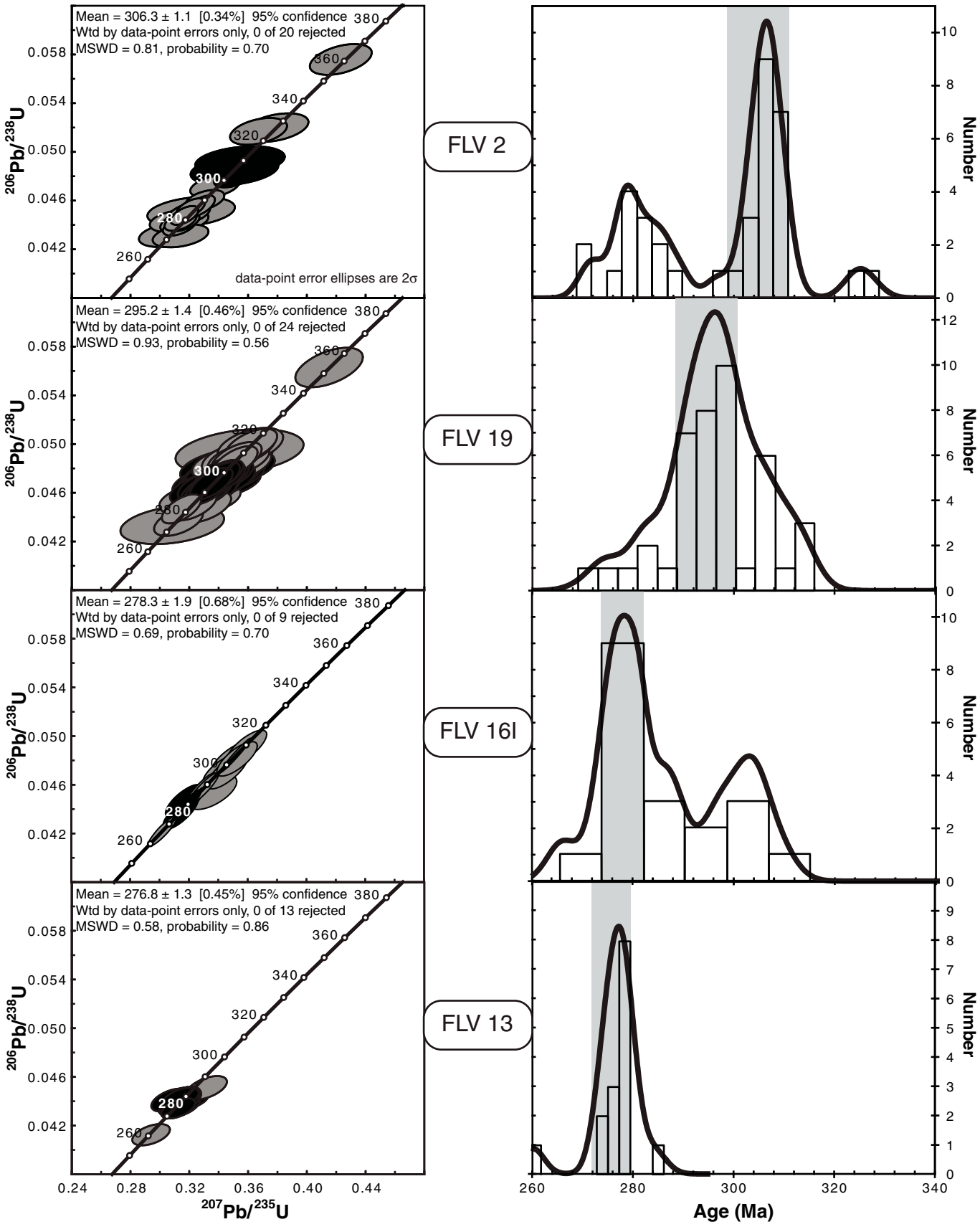

Figure 9. LA-ICP-MS (laser ablation–inductively coupled plasma–mass spectrometer) U/Pb zircon ages plotted on concordia (left column), and density (right column) diagrams. Weighted average ages refer to black ellipses in the concordia diagrams, and to bars in the gray stripes in the density diagrams. MSWD—mean square of weighted deviates.

cause for both processes. As suggested for other locations, the preferred orientation of dikes is strong evidence in favor of a tectonic control on the pattern of brittle discontinuities that favored magma ascent through dikes (e.g., Glazner et al., 1999; Sadeghian et al., 2005; Dini et al., 2008). Following this view, it can be shown that dikes in the Sila Grande are oriented along a geometrically coherent system of brittle discontinuities. The angular relations among the main east-west strike and the four secondary orientations (east-southeast–west-northwest, northwest-southeast, north-northwest–south-southeast, and east-northeast–west-southwest) are shown in Figure 4. It can be seen that east-west strike can be interpreted as a principal displacement zone (Sylvester, 1988), while the secondary orientations can be interpreted as the associated brittle structures: extensional discontinuities, and synthetic or antithetic shears (see Fig. 10) (Petit, 1987; Sylvester, 1988). Thus the Sila Grande network of discontinuities may be related to a tectonic event with a significant horizontal component of dextral simple shear. In addition, to produce tectonic exhumation, a vertical orientation of the principal stress is required for the late Hercynian Calabria continental crust (Caggianelli et al., 2007). Consequently, we propose a dextral transtensional setting as the tectonic framework for Pennsylvanian–Early Permian exhumation and infiltration of magmas in the upper crust. In agreement with this interpretation, the synoptic sketch of Figure 10 depicts the evolution of the continental crust exposed in the Sila Grande from 306 Ma (age of emplacement of the granodiorite) to 277 Ma (age of the latest dike). The block diagram in Figure 10A represents the starting point of the evolution. The plutonics of the Sila Grande occupied the intermediate part of the continental crust. A surface located at a paleodepth of ~13 km is traced on the basis of igneous barometry. The block diagram in Figure 10B is a snapshot of the situation ca. 295 Ma, the age of emplacement of the mafic dikes. The paleosurface, originally located at 13 km, has now reached the shallower level of ~5 km as constrained by barometric estimates on the mafic dike. Exhumation was activated by transtensional tectonics with a dextral component that produced a coherent network of brittle discontinuities, representing a preferential path for magma ascent into the upper crust. The block diagram in Figure 10C represents a more advanced stage of the evolution to 277 Ma, when the network of discontinuities acquired the current extent, and injected magmas were dominantly acidic. Figure 10D reproduces the present situation, after Mesozoic to Cenozoic tectonic episodes responsible for the northeastward tilting of the Sila crustal section.

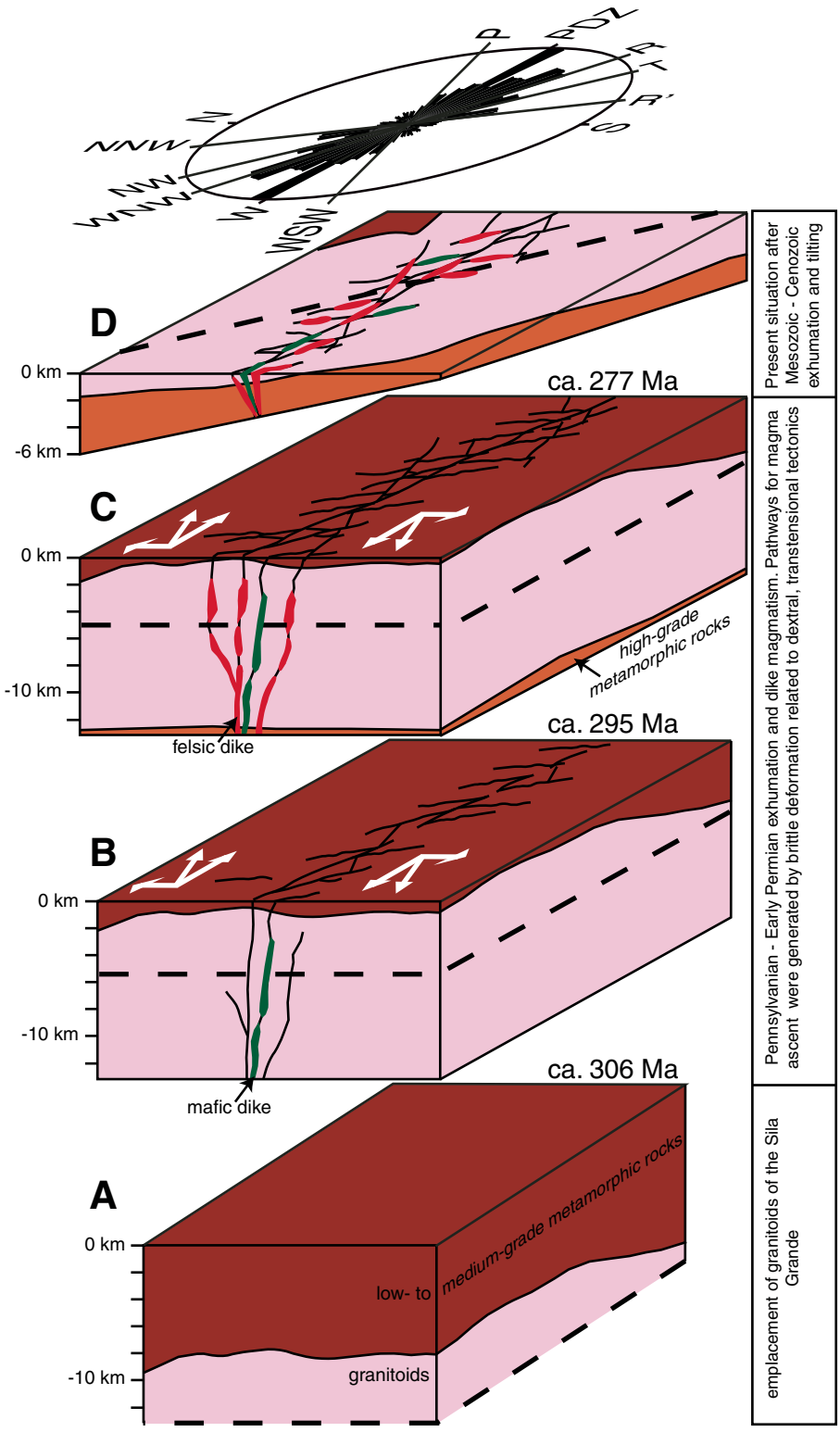

Figure 10. Block diagrams summarizing the exhumation stages of the Sila Grande basement since the Pennsylvanian. Depths from the paleosurfaces (A to C), and from the present surface (D) are indicated in kilometers. The thick dashed line indicates the level of emplacement of granodiorite estimated by geobarometry. The pattern of dike orientations on the top (from Fig. 4) conforms to the array of brittle structures produced by an east-west dextral strike-slip component. PDZ—principal displacement zone; R—Riedel synthetic shears; R′—Riedel antithetic shears; T—extension discontinuities; P—synthetic shears.

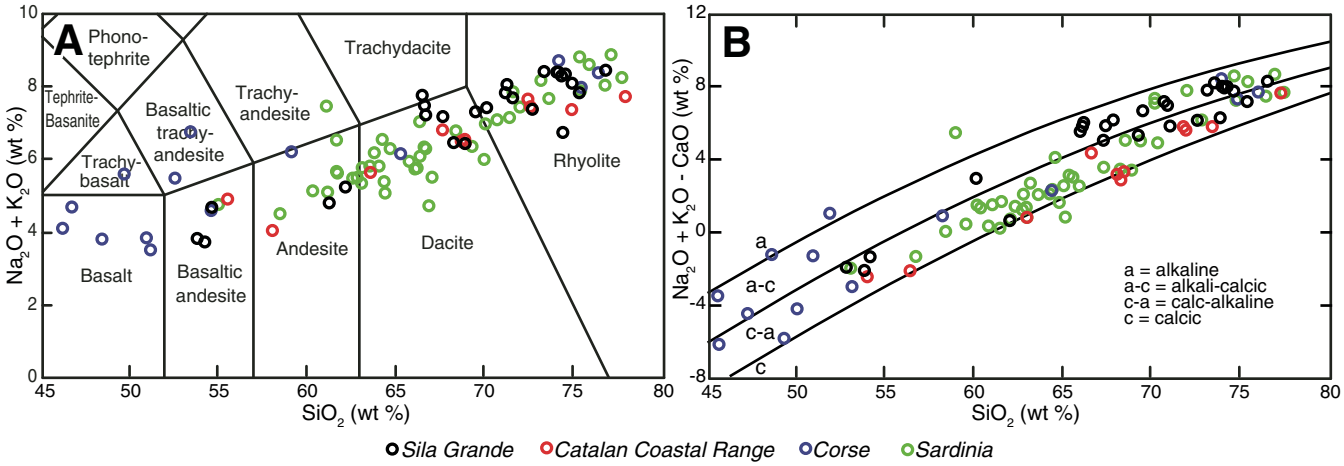

Figure 11. Comparison of the compositional characteristics of the Sila Grande dikes. (A) With those of Catalan Coastal Range, Corse, and Sardinia in the TAS (total-alkali-silica) (Le Bas et al., 1986). (B) In terms of rock series according to the modified alkali-lime index (MALI) by Frost et al. (2001). Sources of data: Enrique (1984, 1990) for the Catalan Costal Range; Atzori et al. (2000) for Sardinia; Traversa et al. (2003) for Corse.

Tectonic processes may be responsible for Pennsylvanian–Early Permian exhumation of the entire Hercynian crust, by dominant ductile thinning in the hot lower levels, and by fracturing in the cool upper levels (Ziegler and Cloetingh, 2003, and references therein).

Regional Significance of Dike Magmatism

The Sila Grande dikes were fed by magmas similar in composition to those found in other pieces of the Hercynian basement now dispersed throughout the central Mediterranean. In Figure 11 data points of the Sila Grande dikes are plotted together with those of dikes from Sardinia, Corse, and the Catalan Coastal Range (Enrique, 1984; Atzori et al., 2000; Traversa et al., 2003). In the TAS diagram (Fig. 11A), data points related to Sila Grande, Sardinia, and Catalan Coastal Range are spread over a wide compositional range, from basaltic andesite to rhyolite. Dikes from Corse display an even larger compositional interval, including basalt dikes with silica content as low as 46 wt%. In terms of the modified alkali-lime index (MALI of Frost et al., 2001), dikes from the selected locations mostly show calc-alkaline to alkali-calcic characteristics (Fig. 11B).

This magmatism took place in a time span from the Pennsylvanian to Early Permian. A close match of the ages in the various regions cannot be established owing to the different dating methods adopted (Ferrés, 1998; Carmignani et al., 1999; Ronca et al., 1999; Atzori et al., 2000; Rossi et al., 2002; Cocherie et al., 2005). Notwithstanding this problem, it can be deduced that most of this magmatic activity affected the southern Hercynian domain between 295 and 270 Ma (Fig. 1). Compositional and timing similarities suggest a common tectonic episode of regional importance was responsible for the widespread Pennsylvanian to Early Permian dike magmatism in the southern Hercynian range.

The dextral transtensional tectonics recognized for the Sila Grande appear to be compatible with Pennsylvanian to Early Permian geodynamical evolution characterized by a major dextral translation between Gondwana and Laurasia (Arthaud and Matte, 1977; Ziegler, 1993), as sketched in Figure 12. This process affected a large region, and was responsible for the clockwise rotation of the European Hercynian belt from ca. 300 to 270 Ma (Stampfli and Borel, 2002; Deroin and Bonin, 2003; Vai, 2003). In

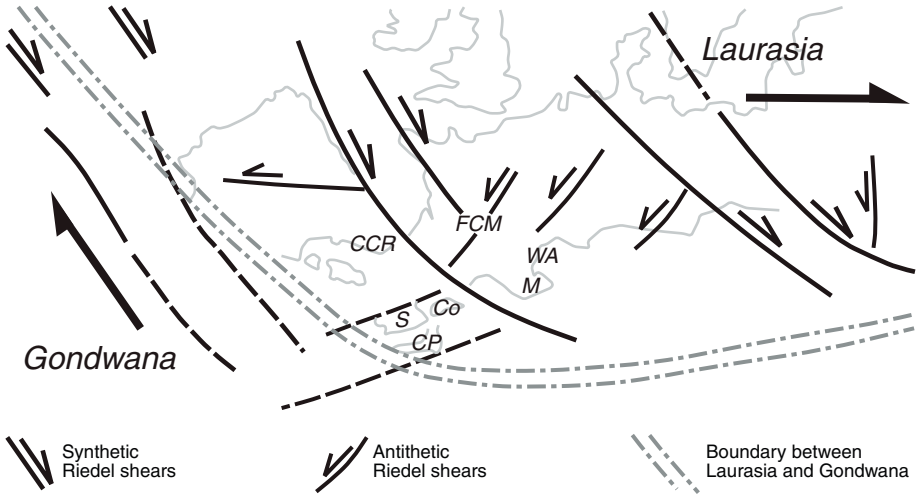

Figure 12. Late Hercynian paleogeography of southern Europe and dextral shear tectonic system between Laurasia and Gondwana (modified from Arthaud and Matte, 1977; Deroin and Bonin, 2003). The original locations of Calabria-Peloritani terrane (CP), Catalan Coastal Range (CCR), Corse (Co), Sardinia (S), French Central Massif (FCM), Western Alps (WA), and Maures Mountains (M) are indicated.

this tectonic context, magmas transitional from calc-alkaline to alkaline series were emplaced in the basement now exposed in the Mediterranean area both as volcanic and plutonic rocks, marking the end of the Hercynian orogenic cycle (e.g., Rossi et al., 1993; Bonin, 1998; Rottura et al., 1998; Orejana et al., 2008).

Dike magmatism in the Sila Grande fits well in this geological scenario and provides further evidence of the Pennsylvanian to Early Permian transtensional regime between Gondwana and Laurasia.

ACKNOWLEDGMENTS

This study was supported by MIUR-PRIN (Ministero Istruzione Università Ricerca–Programmi di Ricerca di Rilevante Interesse Nazionale) 2007 research funds (to R. Spiess, Università degli Studi di Padova, Italy), and Fondi Ateneo (to A. Caggianelli, Università degli Studi di Bari, Italy). We are grateful to P. Enrique and P. Mazzoleni for comments that helped us to improve the manuscript, and to D. Harry and A. Dini for their editorial work. We thank S. Rocchi for his considerable efforts in organizing the LASI III (laccolith and sill conference), and D. Liotta for encouraging discussions on the topics covered in this study.

REFERENCES CITED

Alvarez, W., and Shimabukuro, D.H., 2009, The geological relationships between Sardinia and Calabria during Alpine and Hercynian times: Italian Journal of Geosciences, v. 128, p. 257–268.

Anderson, J.L., and Smith, D.R., 1995, The effects of temperature and oxygen fugacity on the Al-in-hornblende barometer: American Mineralogist, v. 80, p. 549–559.

Arthaud, F., and Matte, P., 1977, Late Paleozoic strike-slip faulting in southern Europe and northern Africa: Result of a right lateral shear zone between the Appalachians and the Urals: Geological Society of America Bulletin, v. 88, p. 1305–1320, doi: 10.1130/0016-7606(1977)88<1305:LPSFIS>2.0.CO;2.

Atzori, P., Cirrincione, R., Del Moro, A., and Mazzoleni, P., 2000, Petrogenesis of late Hercynian calc-alkaline dykes of mid-eastern Sardinia: Petrological and geochemical data constraining hybridization process: European Journal of Mineralogy, v. 12, p. 1261–1282.

Ayuso, R.A., Messina, A., De Vivo, B., Russo, S., Woodruff, L.G., Sutter, J.F., and Belkin, H.E., 1994, Geochemistry and argon thermochronology of the Variscan Sila Batholith, southern Italy: Source rocks and magma evolution: Contributions to Mineralogy and Petrology, v. 117, p. 87–109, doi: 10.1007/BF00307732.

Bertolani, M., 1957, Ricerche sulla natura e sulla genesi delle rocce della Sila (Calabria). Plutoniti e metamorfiti del bacino del Lago Arvo: Bollettino della Società Geologica Italiana, v. 76, p. 79–172.

Bonin, B., 1998, Orogenic to non-orogenic magmatic events: Overview of the late Variscan magmatic evolution of the Alpine belt: Turkish Journal of Earth Sciences, v. 7, p. 133–143.

Boynton, W.V., 1984, Cosmochemistry of rare earth elements: Meteorite studies, *in* Henderson, P., ed., Rare earth elements and geoscience: Amsterdam, Elsevier, p. 63–107.

Burton, A.N., 1970, Carta Geologica Della Calabria, Foglio 237 IV SO Lago Arvo: Cassa per il Mezzogiorno, Servizio Bonifiche, scale 1:25,000, 1 sheet.

Burton, A.N., 1971a, Carta Geologica della Calabria, Foglio 237 IV SE Lago Ampollino: Cassa per il Mezzogiono, Servizio Bonifiche, scale 1:25,000, 1 sheet.

Burton, A.N., 1971b, Carta Geologica della Calabria, Foglio 237 IV NE San Giovanni in Fiore: Cassa per il Mezzogiorno, Servizio Bonifiche, scale 1:25,000, 1 sheet.

Burton, A.N., 1971c, Carta Geologica della Calabria, Foglio 237 IV NO Silvana Mansio: Cassa per il Mezzogiorno, Servizio Bonifiche, scale 1:25,000, 1 sheet.

Caggianelli, A., and Prosser, G., 2001, An exposed cross-section of the late Hercynian and intermediate continental crust in the Sila nappe (Calabria, southern Italy): Periodico di Mineralogia, v. 70, p. 277–301.

Caggianelli, A., Del Moro, A., and Piccarreta, G., 1994, Petrology of basic and intermediate orogenic granitoids from the Sila Massif (Calabria, southern Italy): Geological Journal, v. 29, p. 11–28, doi: 10.1002/gj.3350290103.

Caggianelli, A., Prosser, G., and Di Battista, P., 1997, Textural features and fabric analysis of granitoids emplaced at different depths: The example of the Hercynian tonalites and granodiorites from Calabria: Mineralogica et Petrogrografica Acta, v. 40, p. 11–26.

Caggianelli, A., Del Moro, A., Di Battista, P., Prosser, G., and Rottura, A., 2003, Leucogranite genesis connected with low-pressure high-temperature metamorphism in the Sila basement (Calabria, Italy): Schweizerische Mineralogische und Petrographische Mitteilungen, v. 83, p. 301–316.

Caggianelli, A., Liotta, D., Prosser, G., and Ranalli, G., 2007, Pressure-temperature evolution of the late Hercynian Calabria continental crust: Compatibility with post-collisional extensional tectonics: Terra Nova, v. 19, p. 502–514, doi: 10.1111/j.1365-3121.2007.00777.x.

Carmignani, L., Rossi, P., Barca, S., Durand-Delga, M., Lahondère, D., Oggiano, G., Salvadori, I., Conti, P., Eltrudis, A., Funedda, A., Pasci, S., Cherchi, G.P., Disperati, L., Ferrandini, J., Lahondère, J.-C., Loÿe-Pilot, M.-D., Sarria, E., and Spano, C., 1999, Carta geologica e strutturale della Sardegna e della Corsica: Servizio Geologico d'Italia, Regione Autonoma della Sardegna, BRGM Service Géologique National, Collectivité Territoriale de Corse, scale 1:500,000, 1 sheet.

Cocherie, A., Rossi, P., Fanning, C.M., and Guerrot, C., 2005, Comparative use of TIMS and SHRIMP for U-Pb zircon dating of A-type granites and mafic tholeiitic layered complexes and dykes from the Corsican Batholith (France): Lithos, v. 82, p. 185–219, doi: 10.1016/j.lithos.2004.12.016.

De Fino, M., and La Volpe, L., 1970, I filoni di Rovale (Sila Grande, Calabria): Rendiconti della Società Italiana di Mineralogia e Petrografia, v. 26, p. 517–546.

Deroin, J.P., and Bonin, B., 2003, Late Variscan tectonomagmatic activity in western Europe and surrounding areas: The Mid-Permian episode: Bollettino della Società Geologica Italiana, Special Volume, no. 2, p. 169–184.

Dini, A., Westerman, D.S., Innocenti, F., and Rocchi, S., 2008, Magma emplacement in a transfer zone: The Miocene mafic Orano dyke swarm of Elba Island, Tuscany, Italy, *in* Thomson, K., and Petford, N., eds., Structure and emplacement of high-level magmatic systems: Geological Society of London Special Publication 302, p. 131–148.

Dubois, R., 1976, La suture calabro-apenninique crétacé-éocène et l'ouverture Tyrrhénienne néogène: étude pétrographique et structurale de la Calabre centrale [Ph.D. thesis]: Paris, Université Pierre et Marie Curie, 567 p.

Enrique, P., 1984, The Hercynian post-tectonic plutonic and hypabyssal rocks of the Montnegre Massif, Catalonian Coastal Ranges (NE Spain), *in* Sassi, F.P., and Julivert, M., eds., IGCP Project No. 5 Newsletter, v. 6, p. 45–55.

Enrique, P., 1990, The Hercynian intrusive rocks of the Catalonian Coastal Ranges (NE Spain): Acta Geologica Hispanica, v. 25, p. 39–64.

Ferrés, M., 1998, Géochronologie, pétrogenèse et évolution géochimique des intrusions granitiques alcalines des Chaînes côtières Catalanes dans le cadre du magmatisme hercynien de la Méditerranée nord-occidentale [Ph.D. thesis]: Genève, Université de Genève, 198 p.

Festa, V., Caggianelli, A., Kruhl, J.H., Liotta, D., Prosser, G., Guegen, E., and Paglionico, A., 2006, Late Hercynian shearing during crystallization of granitoid magmas (Sila Massif, southern Italy): Regional implications: Geodinamica Acta, v. 19, p. 185–195, doi: 10.3166/ga.19.185-195.

Franzini, M., Leoni, L., and Saitta, M., 1975, Revisione di una metodologia analitica per fluorescenza-X basata sulla correzione degli effetti di matrice: Rendiconti della Società Italiana di Mineralogia e Petrologia, v. 31, p. 365–378.

Frost, B.R., Barnes, C.G., Collins, W.J., Arculus, R.J., Ellis, D.J., and Frost, C.D., 2001, A geochemical classification for granitic rocks: Journal of Petrology, v. 42, p. 2033–2048, doi: 10.1093/petrology/42.11.2033.

Glazner, A.F., Bartley, J.M., and Carl, B.S., 1999, Oblique opening and noncoaxial emplacement of the Jurassic Independence dike swarm, California: Journal of Structural Geology, v. 21, p. 1275–1283, doi: 10.1016/S0191-8141(99)00090-5.

Graessner, T., and Schenk, V., 2001, An exposed Hercynian deep crustal section in the Sila Massif of northern Calabria: Mineral chemistry, petrology and a P-T path of granulite-facies metapelitic migmatites and metabasites: Journal of Petrology, v. 42, p. 931–961, doi: 10.1093/petrology/42.5.931.

Graessner, T., Schenk, V., Bröcker, M., and Mezger, K., 2000, Geochronological constraints on the timing of granitoid magmatism, metamorphism and postmetamorphic cooling in the Hercynian crustal cross-section of Calabria: Journal of Metamorphic Geology, v. 18, p. 409–421, doi: 10.1046/j.1525-1314.2000.00267.x.

Green, T.H., 1982, Anatexis of mafic crust and high pressure crystallization of andesite, *in* Thorpe, R.S., ed., Andesites: Chichester, John Wiley, p. 465–487.

Gudmundsson, A., 2006, How local stresses control magma-chamber ruptures, dyke injections, and eruptions in composite volcanoes: Earth-Science Reviews, v. 79, p. 1–31, doi: 10.1016/j.earscirev.2006.06.006.

Gudmundsson, A., and Brenner, S.L., 2004, Local stresses, dyke arrest and surface deformation in volcanic edifices and rift zones: Annals of Geophysics, v. 47, p. 1433–1454.

Hanchar, J.M., and Miller, C.F., 1993, Zircon zonation patterns as revealed by cathodoluminescence and backscattered electron images: Implications for interpretation of complex crustal histories: Chemical Geology, v. 110, p. 1–13, doi: 10.1016/0009-2541(93)90244-D.

Holland, T., and Blundy, J., 1994, Non-ideal interactions in calcic amphiboles and their bearing on amphibole-plagioclase thermometry: Contributions to Mineralogy and Petrology, v. 116, p. 433–447, doi: 10.1007/BF00310910.

Horstwood, M.S.A., Foster, G.L., Parrish, R.R., Noble, S.R., and Nowell, G.M., 2003, Common-Pb corrected in situ U-Pb accessory mineral geochronology by LA-MC-ICP-MS: Journal of Analytical Atomic Spectrometry, v. 18, p. 837–846, doi: 10.1039/b304365g.

Le Bas, M.J., Le Maitre, R.W., and Zanettin, B., 1986, A chemical classification of volcanic rocks based on the total alkali-silica diagram: Journal of Petrology, v. 27, p. 745–750.

Liotta, D., Festa, V., Caggianelli, A., Prosser, G., and Pascazio, A., 2004, Mid-crustal shear zone evolution in a syntectonic late Hercynian granitoid (Sila Massif, Calabria, southern Italy): International Journal of Earth Sciences, v. 93, p. 400–413, doi: 10.1007/s00531-004-0385-8.

Liotta, D., Caggianelli, A., Kruhl, J.H., Festa, V., Prosser, G., and Langone, A., 2008, Multiple injections of magmas along a Hercynian mid-crustal shear zone (Sila Massif, Calabria, Italy): Journal of Structural Geology, v. 30, p. 1202–1217, doi: 10.1016/j.jsg.2008.04.005.

Lister, J.R., and Kerr, R.C., 1991, Fluid-mechanical models of crack propagation and their application to magma transport in dykes: Journal of Geophysical Research, v. 96, B6, p. 10049–10077, doi: 10.1029/91JB00600.

Ludwig, K.R., 2003, Isoplot/Ex version 3.0. A geochronological toolkit for Microsoft Excel: Berkeley Geochronology Center Special Publication 4, 70 p.

McDonough, W.F., and Sun, S.-s., 1995, The composition of the Earth: Chemical Geology, v. 120, p. 223–254, doi: 10.1016/0009-2541(94)00140-4.

Miller, E.L., Miller, M.M., Stevens, C.H., Wright, J.E., and Madrid, R., 1992, Late Paleozoic paleogeographic and tectonic evolution of the western U.S. Cordillera, *in* Burchfiel, B.C., et al., eds., The Cordilleran orogen: Conterminous U.S.: Boulder, Colorado, Geological Society of America, Geology of North America, v. G-3, p. 57–106.

Newman, S., and Lowenstern, J.B., 2002, VolatileCalc: A silicate melt–H2O–CO2 solution model written in Visual Basic for excel: Computers & Geosciences, v. 28, p. 597–604, doi: 10.1016/S0098-3004(01)00081-4.

Orejana, D., Villaseca, C., Billström, K., and Paterson, B.A., 2008, Petrogenesis of Permian alkaline lamprophyres

and diabases from the Spanish Central System and their geodynamic context within western Europe: Contributions to Mineralogy and Petrology, v. 156, p. 477–536, doi: 10.1007/s00410-008-0297-x.

Paterson, B.A., Stephens, W.E., and Herd, D.A., 1989, Zoning in granitoid accessory minerals as revealed by backscattered electron imagery: Mineralogical Magazine, v. 53, p. 55–61, doi: 10.1180/minmag.1989.053.369.05.

Petit, J.P., 1987, Criteria for the sense of movement on fault surfaces in brittle rocks: Journal of Structural Geology, v. 9, p. 597–608, doi: 10.1016/0191-8141(87)90145-3.

Ring, U., Brandon, M.T., Willett, S.D., and Lister, G.S., 1999, Exhumation processes, *in* Ring, U., et al., eds., Exhumation processes: Normal faulting, ductile flow and erosion: Geological Society of London Special Publication 157, p. 1–27.

Rittmann, A., 1946, Sulla esistenza di colate riolitiche postalpine in Sila (Calabria): Atti della Accademia Nazionale Dei Lincei, Rendiconti Lincei, Scienze Fisiche e Naturali, v. 1, p. 1026–1027.

Ronca, S., Del Moro, A., and Traversa, G., 1999, Geochronology, Sr-Nd isotope geochemistry and petrology of late-Hercynian dyke magmatism from Sarrabus (SE Sardinia): Periodico di Mineralogia, v. 68, p. 231–260.

Rossi, P., Durand-Delga, M., and Cocherie, A., 1993, Caractère volcano-plutonique du magmatisme calco-alcalin composite d'âge stéphanien supérieur-permien inférieur en Corse: Paris, Académie des Sciences Comptes Rendus, v. 316, p. 1779–1788.

Rossi, P., Cocherie, A., Lahondère, D., and Fanning, C.M., 2002, La marge europeénne de la Téthys jurassique en Corse: datation de trondhjémites de Balagne et indices de croûte continentale sous le domaine balano-ligure: Paris, Académie des Sciences Comptes Rendus v. 334, p. 313–332, doi: 10.1016/S1631-0713(02)01758-3.

Rottura, A., Bargossi, G.M., Caggianelli, A., Del Moro, A., Visonà, D., and Tranne, C.A., 1998, Origin and significance of the Permian high-K calc-alkaline magmatism in the central eastern Southern Alps, Italy: Lithos, v. 45, p. 329–348, doi: 10.1016/S0024-4937(98)00038-3.

Sadeghian, M., Bouchez, J.-L., Nédélec, A., Siqueira, R., and Valizadeh, M.V., 2005, The granite pluton of Zahedan (SE Iran): A petrological and magnetic fabric study of a syntectonic sill emplaced in a transtensional setting: Journal of Asian Earth Sciences, v. 25, p. 301–327, doi: 10.1016/S1367-9120(04)00071-9.

Schenk, V., 1989, P-T-t paths of the lower crust in the Hercynian fold belt of southern Calabria, *in* Daly, J.S., et al., eds., Evolution of metamorphic belts: Geological Society of London Special Publication 43, p. 337–342.

Schmidt, M.W., and Thompson, A.B., 1996, Epidote in calc-alkaline magmas: An experimental study of stability, phase relationships, and the role of epidote in magmatic evolution: American Mineralogist, v. 81, p. 462–474.

Sisson, T.W., Grove, T.L., and Coleman, D.S., 1996, Hornblende gabbro sill complex at Onion Valley, California, and a mixing origin for the Sierra Nevada batholith: Contributions to Mineralogy and Petrology, v. 126, p. 81–108, doi: 10.1007/s004100050237.

Spear, F.S., 1993, Metamorphic phase equilibria and pressure-temperature-time paths: Washington, D.C., Mineralogical Society of America Monograph 1, 799 p.

Stampfli, G.M., and Borel, G.D., 2002, A plate tectonic model for the Paleozoic and Mesozoic constrained by dynamic plate boundaries and restored synthetic oceanic isochrons: Earth and Planetary Science Letters, v. 196, p. 17–33, doi: 10.1016/S0012-821X(01)00588-X.

Sylvester, A.G., 1988, Strike-slip faults: Geological Society of America Bulletin, v. 100, p. 1666–1703, doi: 10.1130/0016-7606(1988)100<1666:SSF>2.3.CO;2.

Tibaldi, A., Vezzoli, L., Pasquaré, F.A., and Rust, D., 2008, Strike-slip fault tectonics and the emplacement of sheet-laccolith systems: The Thverfell case study (SW Iceland): Journal of Structural Geology, v. 30, p. 274–290, doi: 10.1016/j.jsg.2007.11.008.

Tiepolo, M., 2003, In situ Pb geochronology of zircon with laser ablation-inductively coupled plasma-sector field mass spectrometry: Chemical Geology, v. 199, p. 159–177, doi: 10.1016/S0009-2541(03)00083-4.

Traversa, G., Ronca, S., Del Moro, A., Pasquali, C., Buraglini, N., and Barbarino, G., 2003, Late to post-Hercynian dyke activity in the Sardinia-Corsica Domain: A transition from orogenic calc-alkaline to anorogenic alkaline magmatism: Bollettino della Società Geologica Italiana, Special Volume, no. 2, p. 131–152.

Vai, G.B., 2003, Development of the palaeogeography of Pangaea from Late Carboniferous to Early Permian: Palaeogeography, Palaeoclimatology, Palaeoecology, v. 196, p. 125–155, doi: 10.1016/S0031-0182(03)00316-X.

van Achterbergh, E., Ryan, C.G., Jackson, S.E., and Griffin, W., 2001, Data reduction software for LA-ICPMS, in Sylvester, P., ed., Laser ablation ICPMS in the Earth sciences: Principles and applications: Mineralogical Association of Canada Short Course Series Volume 29, p. 239–243.

Vavra, G., 1990, On the kinematics of zircon growth and its petrogenetic significance: A cathodoluminescence study: Contributions to Mineralogy and Petrology, v. 106, p. 90–99, doi: 10.1007/BF00306410.

Wiedenbeck, M., Allé, P., Corfu, F., Griffin, W.L., Meier, M., Oberli, F., Von Quadt, A., Roddick, J.C., and Spiegel, W., 1995, Three natural zircon standards for U-Th-Pb, Lu-Hf, trace elements and REE analyses: Geostandards Newsletter, v. 19, p. 1–23, doi: 10.1111/j.1751-908X.1995.tb00147.x.

Wilson, M., Neumann, E.-R., Davies, G.R., Timmerman, M.J., Heeremans, M., and Larsen, B.T., 2004, Permo-Carboniferous magmatism and rifting in Europe: Introduction, *in* Wilson, M., et al., eds., Permo-Carboniferous magmatism and rifting in Europe: Geological Society of London Special Publication 223, p. 1–10.

Wyllie, P.J., 1978, Water and magma generation at subduction zones: Bulletin of Volcanology, v. 41, p. 360–377, doi: 10.1007/BF02597371.

Ziegler, P.A., and Cloetingh, S., 2004, Dynamic processes controlling evolution of rifted basins: Earth-Science Reviews, v. 64, p. 1–50, doi: 10.1016/S0012-8252(03)00041-2.

Ziegler, P.A., 1993, Late Palaeozoic–early Mesozoic plate reorganization: Evolution and demise of the Variscan Fold Belt, *in* von Raumer, J., and Neubauer, F., eds., The pre-Mesozoic geology in the Alps: Berlin, Springer, p. 203–216.

Manuscript Received 19 January 2010
Revised Manuscript Received 25 May 2010
Manuscript Accepted 9 September 2010